Towards a physically and microstructure-based equation for the evolution of the specific surface area in snow

Anna BRAUN[1,2], Kévin FOURTEAU[3], Simon FREI[1], Michael LEHNING[1,2], Henning LÖWE[1]

[1]*WSL Institute for Snow and Avalanche Research SLF, 7260 Davos Dorf, Switzerland*

[2]*Laboratory of Cryospheric Sciences, School of Architecture, Civil and Environmental Engineering, Ecole Polytechnique Federale de Lausanne, 1015 Lausanne, Switzerland*

[3]*Université Grenoble Alpes, Université de Toulouse, Météo-France, CNRS, CNRM, Centre d'Études de la Neige, Grenoble, France*

Correspondence: Henning Löwe <loewe@slf.ch>

ABSTRACT. The specific surface area (SSA) of snow is a critical structural quantity that controls snow properties and constantly evolves over time. An accurate understanding and modeling of the dynamical evolution of the SSA is thus of primary importance for snowpack models. For this, we simulate the evolution of randomly generated bi-continuous microstructures that resemble real snow microstructures and investigate the control of the ambient conditions (temperature and temperature gradient) and of the physical processes at play on the rate of change of the SSA. Based on this, we propose a new physically-informed governing law for the coarsening of microstructures. This law could also benefit other materials than snow, for instance metal alloys. It involves three new material properties, corresponding to the sensitivity to isothermal and temperature gradient conditions and a length scale controlling the transition from kinetics-limited to diffusion-limited regimes. This law accurately predicts the simulation outputs under various conditions. We also propose a potential parametrization of the three newly introduced material properties and evaluate it against snow coarsening data. This work opens the path to a closed system of physics-based equations governing snow microstructural evolution, with direct applicability in snowpack models.

INTRODUCTION

The specific surface area (SSA) of snow is a critical structural quantity that notably controls the albedo of the snow cover (Grenfell and S.G, 1999; Montpetit and others, 2012) and, therefore, significantly impacts the Earth's energy budget (Flanner and Zender, 2006; Zelinka and Hartmann, 2012). The SSA of snow corresponds to the interfacial area between the ice and air phases per total volume or snow mass. Alongside snow density, the SSA of snow (or direct equivalents such as the optical diameter, for instance) is used in snowpack models to describe the microstructure of the snow layers forming the snowpack (Bartelt and Lehning, 2002; Vionnet and others, 2011). Such models simulate the physical processes at play in the snowpack and predict its state and physical properties. They are used then in support of avalanche forecasting services (Morin and others, 2020), in operational snow-hydrology (Mott and others, 2023), or climate studies (Eckert and others, 2024). In a natural snowpack, the SSA of snow is constantly evolving as the snow microstructure continuously changes its spatial arrangement of the ice and air phases, in a process known as snow metamorphism. Besides snow, the properties of metal alloys, polymers and semiconductors similarly depend on the interfacial area between phases. For instance, the tensile strength of Al-Si alloy decreases as the secondary dendritic arm spacing increases (Osório and others, 2006; P. R. Goulart and Garcia, 2007), which is directly related to the interfacial surface area (Guo and others, 2017). An accurate understanding and representation of the evolution of the SSA over time is thus of primary importance for studies on snow and of general interest for material sciences. Yet, the SSA evolution in present snowpack models remains poorly estimated (Tuzet and others, 2017; Calonne and others, 2020), with direct consequences on the ability to accurately model the physical properties of the snow cover.

Under isothermal conditions, mostly occurring in deep snowpacks, the SSA decreases over time in response to curvature variations and the Gibbs-Thomson effect (i.e., the change of the saturated vapor pressure due to surface curvature). This coarsening corresponds to a reduction of excess free energy at the interface between the two phases. The process of coarsening under curvature effects has been extensively studied under the assumption that the microstructure consists of spherical particles with different radii. This corresponds to the seminal coarsening theory first developed by Lifshitz and Slyozov (1961), and Wagner (1961) (LSW). Overall, the LSW theory predicts that large particles, with lower interfacial curvature, grow at the expense of smaller particles, with high interfacial curvature. Qualitatively, the theory applies to snow (Löwe and others, 2011), but specific features stemming from the bi-continuous nature of the material, might not be captured. Moreover, truly isothermal conditions only represent a small fraction

of the ambient conditions under which snow evolves. Notably, seasonal snowpacks are mostly found under temperature gradient (TG) conditions, due to the temperature difference between the (warm) ground and the (cold) snowpack surface. The work of Snyder and others (1999) highlighted that the presence of a small TG affects the coarsening of an idealized microstructure composed of spheres. Consistently, Taillandier and others (2007) experimentally observed that snow coarsening was faster in TG conditions. Moreover, while the SSA of snow usually decreases over time (Taillandier and others, 2007; Wang and Baker, 2014; Wiese and Schneebeli, 2017), a specificity of the snow evolution under TG conditions is the possibility of an SSA increase (Domine and others, 2009; Pinzer and others, 2012; Wang and Baker, 2014). Therefore, theories of SSA evolution in snow must account for the potential presence of a TG as it can significantly impact the coarsening process. In this idea, Flanner and Zender (2006) proposed a model of snow coarsening meant for both isothermal and TG conditions. It is however based on idealized microstructures composed of non-overlapping spheres rather than actual bi-continuous microstructures. Similarly, Taillandier and others (2007), building on Legagneux and others (2004), proposed a law for coarsening with parametrizations for both isothermal and TG conditions. It assumes a logarithmic decay of the SSA, that can be justified in the case of an isothermal system of isolated spheres (Legagneux and others, 2004). However, the law underestimates the TG case, and the incorporation of the law into the snowpack model could be a reason for the underestimation of the SSA evolution. Understanding and modeling snow metamorphism under TG, in general, and SSA evolution under TG, in particular, still need to be explored.

The last decades have seen the development of X-ray micro-computed tomography (μCT) in snow sciences, which can measure the microstructure and its evolution over time. This enabled studies simulating the physical processes at play at the pore scale in snow microstructures. Several works proposed to model the dynamical evolution of the microstructure itself (e.g. Flin and Brzoska, 2008; Kaempfer and Plapp, 2009; Krol and Löwe, 2016; Braun and others, 2024b). Notably, based on the approach of Drew (1990), Krol and Löwe (2018) derived geometrical evolution equations that can be applied to statistically homogeneous microstructures. This rigorous upscaling approach showed that the evolution of the SSA of a microstructure is directly controlled by the average product of the interface velocity and the interfacial mean curvature. In this picture, the accurate determination of the interface velocity plays a key role. This is consistent with, for instance, the study of Park and others (2015), which pointed out the importance of the interface velocity for the understanding of the complex dynamics of coarsening in bi-continuous structures under curvature effects. In a snow sample, the interface velocity is controlled by the physics responsible for the pore-scale

redistribution of water vapor. These mechanisms are currently globally understood and agreed upon, and include the diffusive transport of water vapor in the pores of snow (Pinzer and others, 2012; Calonne and others, 2014) and the deposition/sublimation of the water vapor at the ice-air interface (Libbrecht, 2005; Fourteau and others, 2021b). These can be modelled with the use of numerical simulations (Kaempfer and Plapp, 2009; Fourteau and others, 2021a; Yan and others, 2022) and the interface velocity derived in the process.

The use of such numerical simulations, combined with the rigorous SSA equation of (Krol and Löwe, 2018), allowed Braun and others (2024b) to simulate the coarsening rate of two samples under TG conditions. The results showed good agreement with experimental data, showcasing the capability of the method to estimate the evolution of the SSA of snow. The simulation work also highlighted the critical role played in the SSA evolution by the condensation coefficient of water vapor onto ice, reflecting how water vapor molecules incorporate into the ice crystal lattice at the ice-air interface (Saito, 1996; Libbrecht, 2005; Fourteau and others, 2020; Libbrecht, 2021; Bouvet and others, 2022). However, the dependence of the condensation coefficient on numerous effects such as temperature, supersaturation, or crystallographic orientation (Saito, 1996; Libbrecht, 2005) and fundamental measurement difficulties (Libbrecht, 2005) hinder the characterization of the condensation coefficient. Translating these uncertainties of the condensation coefficient on the evolution of snow remains an open question.

In this work, we propose to study the coarsening of artificial microstructure using pore-scale simulations and the SSA evolution equation (Krol and Löwe, 2018) in order to quantify the drivers of the SSA evolution in snow. The use of artificially generated microstructures enables fine control of the morphology and thus the systematic investigation of a broad range of microstructures. Section 2 recalls the theoretical background used in this article, i.e., the SSA evolution equation and the physics governing the deposition/sublimation of vapor within microstructures. Section 3 then presents the methods employed in our work, specifically the generation of artificial microstructures and the numerical simulations. Finally, Section 4 analyses the physical drivers of the SSA evolution (temperature, TG, condensation coefficient, etc.), proposes a general law to capture the rate of change of SSA in various microstructures under ambient conditions and evaluates the law based on a series of snow μCT images obtained under controlled TG conditions.

THEORETICAL BACKGROUND

As our main motivation comes from understanding snow metamorphism, we adopt the usual framework of snow sciences. We characterize the microstructures in terms of so-called microstructural descriptors (also sometimes referred to as microstructural properties). These microstructural descriptors are a set of scalars meant to characterize the microstructure. They are well-defined at the macroscopic scale (i.e., the scale of a snow layer) and can thus be used in snowpack models to characterize the snow material. They include the ice volume fraction ϕ_i and the SSA (and potentially others). In this article, we use two definitions of the SSA. For a given microstructure, we define the s as the surface of the ice-air interface per total volume (including the ice and air phases), namely

$$s = \frac{S}{V} \tag{1}$$

with S the surface of the ice-air interface and V the total volume of the microstructure. This definition enables us the direct link to the geometrical evolution of the microstructure via the SSA evolution equation (Krol and Löwe, 2018).

Historically, snow sciences have rather defined the SSA as the surface of the ice-air interface per total mass of the snow sample (e.g., Calonne and others, 2020; Martin and Schneebeli, 2023). To enable a direct comparison with previous snow studies, we further define SSA_M as the surface of the ice-air interface per snow mass. SSA_M is directly related to s through the product of the ice volume fraction ϕ_i and the density of ice ρ_i:

$$SSA_M = \frac{s}{\phi_i \, \rho_i} \tag{2}$$

The aim of the article is to investigate the evolution of s over time. For this purpose, we rely on the upscaled SSA evolution equation derived by Krol and Löwe (2018). It relates the rate of change of s to the velocity field at the ice-air interface within a microstructure. Neglecting the mechanical deformation of the ice matrix, this equation reads as

$$\dot{s} = 2 \, s \, \overline{v_{\mathbf{n}} H} \tag{3}$$

where $\dot{s}$ is the time derivative of the s, $v_{\mathbf{n}}$ is the normal velocity of the ice-air interface (due to the deposition and sublimation of water vapor), H is the mean curvature of the ice-air interface, and the operator $\overline{\bullet}$ stands for the average over the ice-air interface. As classically done with homogenization methods, this equation links the microscopic fields $v_{\mathbf{n}}$ and H (defined at each point of the ice-air interface in the microstructure)
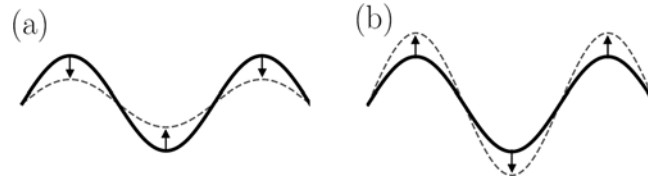
Fig. 1. Geometrical interpretation of the sign of $v_{\mathbf{n}}H$ and of the evolution of the SSA, inspired by Drew (1990). (a) Case of a negative sign, where vapor sublimates in convex zones and deposes in concave zones, leading to a decrease of the SSA. (b) Case of a positive sign, where vapor sublimates in concave zones and deposes in convex zones, leading to an increase of the SSA.

and the macroscopic quantity s through the use of surface averaging. We note that Eq. (3) is not limited to snow and applies to any bi-phasic material. The quantity $\overline{v_{\mathbf{n}}H}$, referred to as the growth rate for the rest of the article, plays a central role. It results from the complex interplay between the movement of water vapor in the microstructure and the local curvature of the microstructure. It corresponds to the relative rate of increase of s, modulo a constant factor 2. A simple geometrical interpretation of the sign of $v_{\mathbf{n}}H$ is displayed in Fig 1. A negative sign of $v_{\mathbf{n}}H$ indicates that vapor sublimates in convex zones and deposes in concave zones. As illustrated in panel a of Fig. 1, such a sublimation/deposition pattern erodes crests and fills troughs in the microstructure, leading to a flattening of the surface and a decrease of the SSA. Conversely, as seen in panel b of Fig. 1, a positive sign of $v_{\mathbf{n}}H$ indicates that crests and troughs are reinforced, leading to an increase of the SSA.

While the curvature field H is fully characterized by the microstructure itself, the interface velocity $v_{\mathbf{n}}$ depends on the external conditions and physical processes at play. It notably varies with the temperature and the TG to which the sample is subjected. This dependence occurs through the physics governing the movement and deposition/sublimation of water vapor in the microstructure. To model this physics, we follow the typical assumption of a small Péclet number at the pore-scale (Libbrecht, 2005), and thus employ the stationary heat and vapor diffusion equations. The water vapor concentration ρ_{v} (expressed in $\mathrm{kg\,m^{-3}}$) and temperature T (K) fields within a microstructure are thus governed by the following system

of equations:

$$
\begin{cases}
\nabla^2 T_{\mathrm{a}} = 0 & \text{in } \Omega_a \\[2mm]
\nabla^2 T_{\mathrm{i}} = 0 & \text{in } \Omega_i \\[2mm]
\nabla^2 \rho_{\mathrm{v}} = 0 & \text{in } \Omega_a \\[2mm]
T_{\mathrm{i}} = T_{\mathrm{a}} & \text{on } \Gamma \\[2mm]
\kappa_i \mathbf{n} \cdot \nabla T_{\mathrm{i}} = \kappa_a \mathbf{n} \cdot \nabla T_{\mathrm{a}} & \text{on } \Gamma \\[2mm]
\nabla \rho_{\mathrm{v}} \cdot \mathbf{n} = \frac{\alpha \, v_{\mathrm{kin}}}{D_{\mathrm{v}}} [\rho_{\mathrm{v}} - \rho_{\mathrm{v,s}}(1 + d_0 \, H)] & \text{on } \Gamma
\end{cases}
\tag{4}
$$

where Ω_a, Ω_i, Γ and $\mathbf{n}$ correspond to the pore space, the ice space, the ice-air interface and the unit normal vector oriented into the pores. T_{a} and T_{i} correspond to the temperatures in the air and the ice, respectively. D_{v} denotes the diffusion coefficient of water vapor in air, κ_a and κ_i the thermal conductivities in the air and the ice, respectively, α the condensation coefficient of water vapor onto ice, v_{kin} the so-called kinetic velocity (Saito, 1996; Libbrecht, 2005; Fourteau and others, 2021b), $\rho_{\mathrm{v,s}}$ the saturated water vapor concentration over a flat surface, d_0 the capillary length, and H the local mean curvature. The system of Eqs. (4) needs to be complemented with appropriate boundary conditions on the side of the simulated domain, characterizing the temperature and TG to which the snow sample is subjected to.

The capillary length d_0 controls the magnitude of the Gibbs-Thomson effect, i.e., the increase (respectively decrease) of the saturated vapor concentration above convex (respectively concave) ice surfaces. It therefore plays a crucial role in isothermal metamorphism, where the redistribution of water vapor at the pore scale is controlled by the curvature effects. It is related to the interfacial energy of ice through $d_0 = \gamma \, a_{\mathrm{is}}^3/(k_{\mathrm{B}} \, T)$, where γ is the interfacial free energy, a_{is} is the mean intermolecular spacing of water molecules in ice and k_{B} is the Boltzmann constant. The product αv_{kin} governs the dynamics at which oversaturated (respectively undersaturated) water vapor is deposited on (respectively sublimated from) an ice surface. The condensation coefficient α corresponds to the probability that a water molecule colliding on the ice crystal surface stays incorporated and the kinetic velocity is given by $v_{\mathrm{kin}} = \sqrt{k_{\mathrm{B}} \, T/(2 \, \pi \, m)}$ with the mass of water molecule m (Saito, 1996; Libbrecht, 2005; Fourteau and others, 2021b). Finally, note that for simplicity, the system of Eqs. (4) neglects the impact of the water vapor latent heat on the temperature. This assumption results in an overestimation of the vapor fluxes within the microstructure, as the effect of latent heat is to decrease the TG within the air phase. Yet, this overestimation of the vapor fluxes likely remains small (Flanner and Zender, 2006; Fourteau and others, 2021a). This is supported by

Braun and others (2024b), which reports a good agreement between experimental data and simulations neglecting the impact of water latent heat. Under this assumption, the system of equations is thus one way-coupled, the temperature influencing the vapor field, but not the other way around.

The system of Eqs. (4) governs the field of water vapor deposition and sublimation, from which the interface velocity $v_{\mathbf{n}}$ can be derived as

$$v_{\mathbf{n}} = \frac{D_{\mathrm{v}} \, \nabla \rho_{\mathrm{v}} \cdot \mathbf{n}}{\rho_{\mathrm{i}}} = \frac{\alpha \, v_{\mathrm{kin}}[\rho_{\mathrm{v}} - \rho_{\mathrm{v,s}}(1 + d_0 \, H)]}{\rho_{\mathrm{i}}} \tag{5}$$

As the interface velocity reflects the movement of the ice-air interface within the microstructure, it has a central meaning for the coarsening process (Park and others, 2015). Again, while Eqs. (4)-(5) are given here for snow, they could be used to model other bi-phasic materials. Finally, we note that the obtained interface velocity field, and hence obtained growth rate, corresponds to a snapshot value on a given microstructure and that microstructural changes are not simulated in this FEM framework. This work assumption is supported by the separation of time-scale between the rapid heat and vapor processes in the microstructure and the slow evolution of the microstructure.

METHODS

As the temporal evolution of the SSA is controlled by the growth rate $\overline{v_{\mathbf{n}}H}$, we set up a workflow to derive it from numerical simulations directly performed at the microstructure-scale. This section aims to present the microstructures used in the article and the specificities of the numerical simulations.

GRF microstructures

Generation of the microstructures

For this study, we explore a range of microstructures, in order to quantify the evolution of the coarsening process for various values of density and SSA. To obtain microstructures spanning a broad range of microstructural characteristics, we rely on artificially generated microstructures using a Gaussian Random Field (GRF) technique. Microstructures generated from GRFs are, for instance, regularly employed in material sciences to study the electromagnetic and elastic properties of porous structures (Roberts and Garboczi, 2002; Ding and others, 2010; Tan and others, 2016; Soyarslan and others, 2018; Blatny and others, 2021, 2023). The generation of GRFs follows the description of Roberts and Teubner (1995), based

on a Gaussian spatial correlation function $G(\boldsymbol{r})$, $\boldsymbol{r}$ being the vector of position. For this study, we use an extended version, which includes a potential spatial anisotropy along the vertical z-axis. Specifically, we construct the correlation function G as a T-periodic Fourier series

$$G(\boldsymbol{r}) = \sum_{l,m,n=-N}^{N} c_{lmn}\,\exp(i\boldsymbol{k}_{lmn}\boldsymbol{r}) \tag{6}$$

where N is the size of the generated sample and $\boldsymbol{k}_{lmn} = 2\pi/N\,(l\hat{\boldsymbol{k}}_x + m\hat{\boldsymbol{k}}_y + n\hat{\boldsymbol{k}}_z)$. The real and imaginary parts of complex coefficients $c_{lmn} = a_{lmn} + ib_{lmn}$ are taken as Gaussian distributed independent random variables with expected values $< a_{lmn} >=< b_{lmn} >= 0$. Their variance is derived from the spectral density $\rho(\boldsymbol{k})$ of the correlation function

$$< a_{lmn}^2 >=< b_{lmn}^2 >= \frac{1}{2}\rho(\boldsymbol{k}_{lmn})\left(\frac{2\pi}{3}\right)^3 \tag{7}$$

Specifically, we assume the correlation function to be Gaussian, i.e.

$$G(\boldsymbol{r}) = \exp(-\frac{r_x^2 + r_y^2}{\sigma^2} - \frac{r_z^2}{a^2\sigma^2}) \tag{8}$$

with σ controlling the standard deviation of the Gaussian correlation function and a an anisotropy ratio along the z-axis. A value of $a > 1$ corresponds to a vertically elongated microstructure, while $a < 1$ corresponds to a microstructure with a preferentially horizontal orientation. Note that the inclusion of anisotropy slightly differs from that by Tan and others (2016), as an isotropic function with a prefactor based on inclination angle is used there instead. The associated spectral density is

$$\rho(\boldsymbol{k}) = \left(\frac{\sigma}{\sqrt{4\pi}}\right)^3 \exp(\frac{-\sigma^2}{4}(k_x^2 + k_y^2 + a^2k_z^2)) \tag{9}$$

Once, the coefficients a_{lmn}, b_{lmn} have been randomly generated, the bi-continuous two-phase microstructure $\mu(\boldsymbol{r})$ is generated by a level-cut:

$$\mu(\boldsymbol{r}) = \begin{cases} \text{ice,} & \text{if } G(\boldsymbol{r}) > l \\ \text{pore,} & \text{otherwise} \end{cases} \tag{10}$$

where l is a parameter that is to be adjusted to yield the desired ice volume fraction. Following the
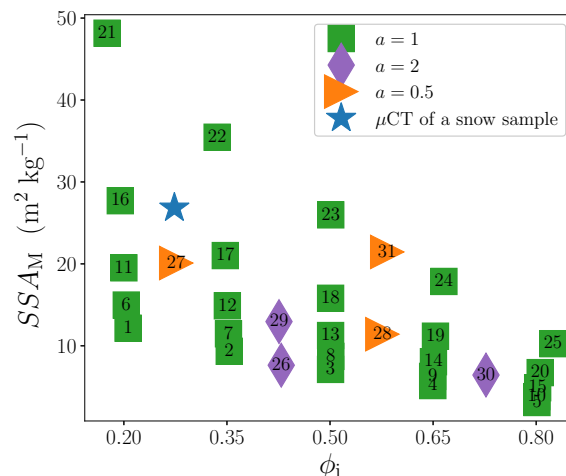
Fig. 2. The ice volume fraction ϕ_i and the SSA SSA_M of the GRF ensemble. Each number corresponds to a GRF microstructure. For a comparison, ϕ_i and SSA_M of a μCT image of a real snow sample that is presented in Fig. 3 are shown.

study by Roberts and Knackstedt (1996), the ice volume fraction ϕ_i of the microstructure can be directly related to l as

$$\phi_i = \frac{1}{\sqrt{2\pi}} \int_{u=l}^{\infty} \exp\left(-\frac{u^2}{2}\right) du. \tag{11}$$

Therefore, by varying the input parameters l, σ, and a, we can produce microstructures with various microstructural properties. The obtained microstructure is defined on a voxel basis, similar to μCT images. We assume a voxel size of $18 \cdot 10^{-6}$ m for the GRF microstructures, the same voxel size as for the snow sample presented below and visualized in Fig. 3. For the present study, we generated 25 isotropic ($a = 1$) and 6 anisotropic ($a = 0.5$ or 2) GRF microstructures with ice volume fraction ϕ_i ranging from 0.21 to 0.83 (density ranging from 190 to $760\,\mathrm{kg\,m^{-3}}$) and SSA_M ranging from 3 to $48\,\mathrm{m^2 kg^{-1}}$. The ensemble of 31 generated microstructures is presented in Fig. 2 by their ice volume fraction and SSA, in which each number identifies a GRF microstructure. In the following, we refer to these numbers to specify the GRF microstructures (also called GRFs) and to the ensemble of generated microstructures as the GRF ensemble. The structural variety of the GRF ensemble is illustrated in Fig. 3 by some GRF microstructures.

Qualitative comparison to real microstructures

While artificial in nature, the generated GRFs are meant to emulate the microstructures of natural material. In particular, the GRFs with low ice volume fraction ($\phi_i \leqslant 0.5$) will be used to study the SSA evolution
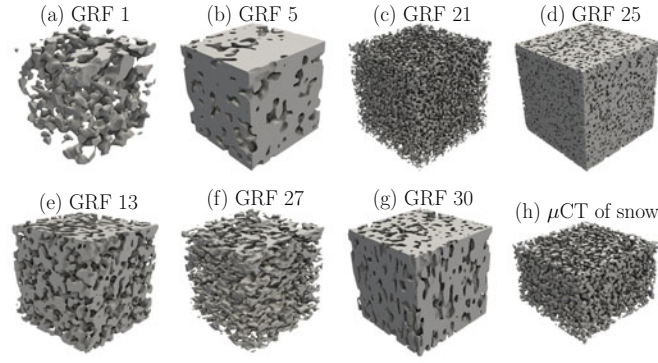
Fig. 3. Visualization of some GRF microstructures from the GRF ensemble and a μCT of a real snow microstructure.

of snow and are thus meant to share similarities with it. Due to the nature of GRFs, the generated microstructures present relatively rounded shapes, akin to those found in rounded grains (RG) or melt forms (MF) in snow (following the classification of Fierz and others, 2009). For comparison, an actual fine RG snow microstructure acquired by μCT (from Pinzer and others, 2012) is displayed in Fig. 3h. This snow microstructure has a ice volume fraction of $\phi_i = 0.27$ and $SSA_M = 27$ m^2 kg^{-1}. Typically for snow, SSA_M ranges from around 8 to 50 m^2 kg^{-1} (Meloche and others, 2022; Martin and Schneebeli, 2023), a similar range as the one of the GRF generated for this study. Moreover, as seen visually, the morphology of the actual snow microstructure resembles that of the artificial microstructures. Similarly, the GRFs generated with high ice volume fraction ($\phi_i > 0.5$) resemble the type of microstructures found in polar firn, with rounded bubbles and pores enclosed in a dense ice matrix (e.g., Freitag and others, 2004; Burr and others, 2018).

Numerical simulations

The first step of our simulation workflow is designed to provide reliable solutions of heat and mass transport within a microstructure and to derive the deposition/sublimation of water vapor at the ice-air interface (Krol and Löwe, 2016; Braun and others, 2024b). For this, the system of Eqs. (4) needs to be solved on an accurate representation of the microstructure. We employ the finite element method (FEM), following the numerical scheme presented in (Braun and others, 2024b). A tetrahedral finite element mesh of the microstructure is generated with the Computational Geometry Algorithms Library (CGAL). In order to properly model the ice-air interface, we first represent the interface as a smooth polyhedral surface and then use the class `Polyhedral_mesh_domain_with_features_3` of CGAL, which preserves the surface during

tetrahedral meshing. Preserving the ice-air interface is particularly relevant for the computation of the growth rate extracted from that surface. The size of finite elements (tetrahedra and triangles) is controlled by various meshing criteria. The impact of the meshing criteria on the growth rate is assessed below.

The open-source software for multiphysics Elmer FEM (Malinen and Råback, 2013) is used to solve the stationary heat and vapor diffusion equations on the finite element mesh. The average temperature T_{mid} and the macroscopic TG across the microstructure ∇T are specified by imposing the top and bottom temperature of the sample as in (Braun and others, 2024b). In the simulations, the values for v_{kin} and D_{v} are taken as constant, while the values for α and d_0 are taken in the ranges $\left[10^{-6} - 10^2\right]$ and $\left[0\,\text{m} - 10^{-9}\,\text{m}\right]$, respectively. Specifically, the value for the kinetic velocity is set to $v_{\text{kin}} = 140\ \text{m}\,\text{s}^{-1}$ (corresponding to $T \approx -5\,^{\circ}C$) and that of the diffusion coefficient of vapor to $D_v = 2 \cdot 10^{-5}\,\text{m}^2\,\text{s}^{-1}$. Note that since v_{kin} and D_{v} only appear in the product $\frac{\alpha v_{\text{kin}}}{D_{\text{v}}}$ in the boundary condition at the ice-air interface (cf., Eq. (4)), the variations of v_{kin} or D_{v} are equivalent to variations of α. The assumption that v_{kin} and D_{v} are constant therefore does not lead to a loss of generality for the solution of the vapor field. We further assume that the saturated vapor concentration over a flat interface follows the Clausius-Clapeyron condition:

$$\rho_{\text{v,s}}(T) = \frac{m}{k_{\text{B}}\,T}P_0 \exp\left(\frac{L_{\text{fus}}}{k_{\text{B}}}\left(\frac{1}{T_0} - \frac{1}{T}\right)\right) \tag{12}$$

with $T_0 = 273.15\,\text{K}$ a reference temperature, $P_0 = 611\,\text{Pa}$ the saturated water vapor pressure over ice at T_0, and $L_{\text{fus}} = 8.37 \cdot 10^{-20}\,\text{J}$ the latent heat of sublimation per molecule of water.

The solution of the heat and vapor diffusion simulation yields the field of water vapor deposition and sublimation, from which the interface velocity $v_{\mathbf{n}}$ can be derived using Eq. (5). The growth rate is then finally obtained, as the product of the v_{n} and H fields averaged over the ice-air interface in the FEM mesh. For these computations, we employed the Visualization Toolkit (VTK) (Schroeder and others, 2006).

Validation of the numerical workflow

The use of FEM simulations to derive the interface velocity and the growth rate has recently been used in (Braun and others, 2024b). This previous work validated the use of this method to reproduce the growth rate of an idealized spherical microstructure. Furthermore, the method was capable of simulating the SSA evolution of two snow samples under TG conditions. However, to achieve such results it was important that (i) the simulated domain was large enough to be representative of the snow metamorphism process and
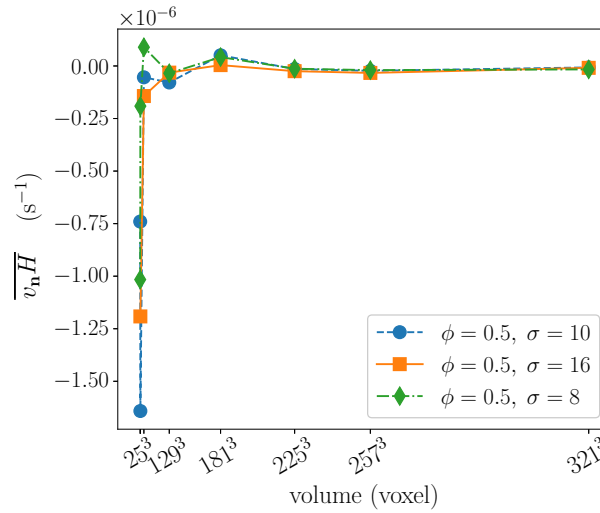
Fig. 4. Dependence of the simulated growth rate on the size of the evaluated microstructure. These computations were performed to determine the REV size by around 225^3 voxels.

(ii) that the mesh was refined enough to yield accurate water vapor fields. These two points are discussed below for the current study.

Representative elementary volume

The determination of a representative elementary volume (REV) is essential to derive meaningful results in the study of complex, heterogeneous materials. The REV is defined as the minimum volume of a sample from which a given property becomes independent of the size of the sample (Bear and Bachmat, 2012). We define the REV in terms of the growth rate $\overline{v_{\mathbf{n}} H}$. The REV is determined by performing simulations on varying sub-volumes of some GRF structures, with a maximal size-length of 512 voxels (corresponding to 9.2 mm). The dependence of the growth rate on the sample sizes is shown in Fig. 4. It suggests that the REV of the GRF microstructures concerning the growth rate is around 225^3 voxels. Thus, for all later presented results, the simulations were carried out on volumes of 260^3 voxels, above the REV limit. It's consistent with the REV sizes determined by Braun and others (2024b) for the growth rate of snow.

Spatial discretization error

Besides determining the sensitivity of the growth rate to the microstructure size, the control of the spatial discretization error is evaluated. The use of a very refined mesh is expected to yield the most accurate results, but at the expense of a high numerical cost. To ensure the use of a sufficiently refined mesh while keeping a reasonable number of elements, we performed simulations with different degrees of mesh
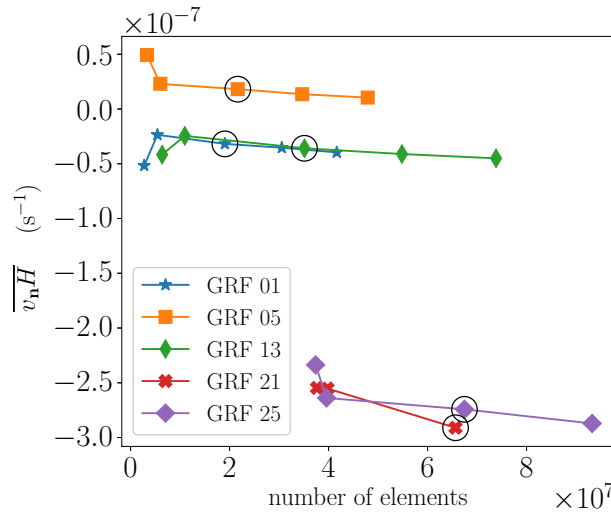
Fig. 5. Impact of the mesh refinement on the simulated growth rate for some extreme cases of GRF microstructures ensemble. Circles indicate the number of elements used in the rest of the article.

refinement. Specifically, we used the meshing criteria to resize the tetrahedra and surface triangles. As shown in Fig. 5, doubling the number of elements in the finite element mesh impacted the growth rate $\overline{v_{\mathbf{n}}H}$ by about 10 %. This indicates a rather small dependence on the mesh considering the impact of numerical parameters on the growth rate examined in the next section. The sensitivity analysis emphasizes that the outlined workflow is suitable for investigating the drivers of the SSA evolution.

Performed simulations

Obtaining the growth rate $\overline{v_{\mathbf{n}}H}$ is the end goal of our numerical workflow, which starts from a GRF microstructure, performs numerical simulations of heat and water vapor diffusion in the microstructure and finally extracts the growth rate. Using the GRF ensemble allows us to evaluate the impact of the microstructure morphology on the growth rate. Similarly, varying the boundary conditions of the simulations reveals the role of the temperature and TG on the SSA evolution. The workflow also offers the possibility to investigate the role of the pore-scale physics (i.e., the condensation coefficient α or the capillary length d_0) on the growth rate.

We performed simulations with average temperatures T_{mid} ranging from 233 to 273 K and with TGs ∇T from 0 to 100 Km^{-1}. To investigate the sensitivity to the pore-scale physics, which remains poorly constrained, we varied the condensation coefficient α between 10^{-6} and 10^2 and the capillary length d_0 between 0 and 10^{-9} m. The upper range of α above unity is taken in order to investigate conditions with

highly reactive interfaces. As mentioned above, the values of v_{kin} and D_{v} are assumed to be constant. The broad range of numerical simulations resolves various conditions and enables the assessment of dependencies of the growth rate.

RESULTS AND DISCUSSION

What drives the coarsening of a microstructure?

The goal of this section is to analyze the drivers of the coarsening of microstructures under both isothermal and TG conditions, and to analyze the differences of coarsening between microstructures.

Based on the system of Eqs. (4) and its boundary conditions, there are four main controls on the growth rate of a microstructure: the average temperature, the TG, the condensation coefficient α (and more generally, the reactivity of the ice-air interface described by the product $\alpha\,v_{\mathrm{kin}}$), and the capillary length d_0. Here, we thus investigate the role of these four parameters on the growth rate.

Macroscopic temperature gradient

We start with the role of the TG across the microstructure. The magnitude of the TG is expected to control the transition between isothermal metamorphism (∇T close to $0\,\mathrm{K\,m^{-1}}$) and TG metamorphism (large ∇T). For that, we used simulations with TG ∇T varying from 0 to $100\,\mathrm{K\,m^{-1}}$ and with the other parameters being fixed ($T_{\mathrm{mid}} = 265.55\,\mathrm{K}$, $\alpha = 10^{-2}$, and $d_0 = 10^{-9}\,\mathrm{m}$ as in (Braun and others, 2024b)). Figure 6 displays the impact of the ∇T on the growth rate $\overline{v_{\mathbf{n}}H}$. For better readability, we do not show the results for all microstructures in the figure, but only for a selection of microstructures, which are representative of the overall GRF ensemble. The graph shows a linear dependence between the growth rate and the TG. Yet, the different microstructures reveal a broad range of behaviors, with some microstructures showing coarsening (i.e., $\overline{v_{\mathrm{n}}H} < 0$) or increase in SSA ($\overline{v_{\mathrm{n}}H} > 0$). Notably, there is a distinction between microstructures with $\phi_{\mathrm{i}} > 0.5$ and $\phi_{\mathrm{i}} \leqslant 0.5$, the latter being typical for snow. For the microstructures with low ice volume, an increase of ∇T leads to a more pronounced coarsening, while in denser microstructures an increase of ∇T leads to hindered coarsening (or even an increase of the SSA). Finally, a high SSA appears to be linked with a lower influence of the TG, with some high SSA microstructures even showing almost no dependence of the growth rate on ∇T.

The linear dependence of the growth rate on the TG is to be expected, at least with strong TGs when the TG regime is well established. Indeed, in this case, the local influence of temperature on the

fluctuation of the saturated water vapor concentration at the ice-air interface overrides the influence due to the local curvature. For the system of Eqs. (4), the dominance of local temperature implies that the last equation can be replaced by $\mathbf{n} \cdot \nabla \rho_{\mathrm{v}} = \frac{\alpha\, v_{\mathrm{kin}}}{D_{\mathrm{v}}} [\rho_{\mathrm{v}} - \rho_{\mathrm{v,s}}(T)]$. Moreover, under the assumption of separation between the microscopic (pore size) and macroscopic (microstructure size) scales, the saturated vapor can be linearized, i.e., $\rho_{\mathrm{v,s}}(T) = \rho_{\mathrm{v,s}}(T_{\mathrm{mid}}) + \beta(T_{\mathrm{mid}})\,(T - T_{\mathrm{mid}})$, with $\beta(T)$ the derivative of the saturated vapor with respect to the temperature. Under this condition, the fluctuations of the field $\rho_{\mathrm{v,s}}(T)$ becomes directly proportional to ∇T, since the fluctuations of T are proportional to ∇T (e.g., Moyne and others, 1988; Calonne and others, 2014). The field $\rho_{\mathrm{v,s}}$ is then composed of an average value $\rho_{\mathrm{v,s}}(T_{\mathrm{mid}})$ and a spatially fixed pattern proportional to ∇T. In these circumstances, the water vapor deposition/sublimation, and hence the interface velocity $v_{\mathbf{n}}$, becomes directly proportional to the macroscopic TG. Yet, for three microstructures with high SSA, the dependence on ∇T is very small (notably visible as horizontal curves in Fig. 6), and shows a quadratic form (rather than a straight line). This peculiar behavior (in disagreement with linear behavior expected when the TG regime is well established) could be due to interactions between the TG and the curvature influence of the vapor field inside the microstructures. The TG regime on these microstructures could be better established at very high ∇T. Apart from these exceptions for the microstructures with high SSA and minor changes in the growth rate, the dependence of the growth rate on the TG seems to be well represented by the linear function. The linear relation could, therefore, be used as the first approximation to estimate the contribution of TG to the growth rate.

Average Temperature

A second important control on SSA evolution is the average temperature of the sample. In the system of Eqs. (4), the average temperature mainly contributes to the growth rate via the saturated vapor $\rho_{\mathrm{v,s}}$ in the Robin boundary condition at the ice-air interface. The specific impact of the average temperature is different depending on whether isothermal or TG metamorphism is at play.

In the isothermal case, the boundary condition at the ice-air interface simply is $\mathbf{n} \cdot \nabla \rho_{\mathrm{v}} = \frac{\alpha\, v_{\mathrm{kin}}}{D_{\mathrm{v}}} [\rho_{\mathrm{v}} - \rho_{\mathrm{v,s}}(T_{\mathrm{mid}})(1 + d_0 H)]$. Linearizing $\rho_{\mathrm{v,s}}(T)$ as in the above discussion on ∇T, the field $\rho_{\mathrm{v,s}}(T)(1 + d_0 H)$ is formed by an average value $\rho_{\mathrm{v,s}}(T_{\mathrm{mid}})$ and the spatial pattern $\rho_{\mathrm{v,s}}(T_{\mathrm{mid}})d_0 H$. The interface velocity is proportional to these spatial fluctuations. Thus, in the isothermal case, the growth rate inherits the dependence of $\rho_{\mathrm{v,s}}$ on the average temperature T_{mid}. Thus, in the isothermal case, $v_{\mathbf{n}}$ and the growth rate $\overline{v_{\mathbf{n}} H}$ inherit the dependence of $\rho_{\mathrm{v,s}}$ on the average temperature T_{mid}. The linear dependence of the
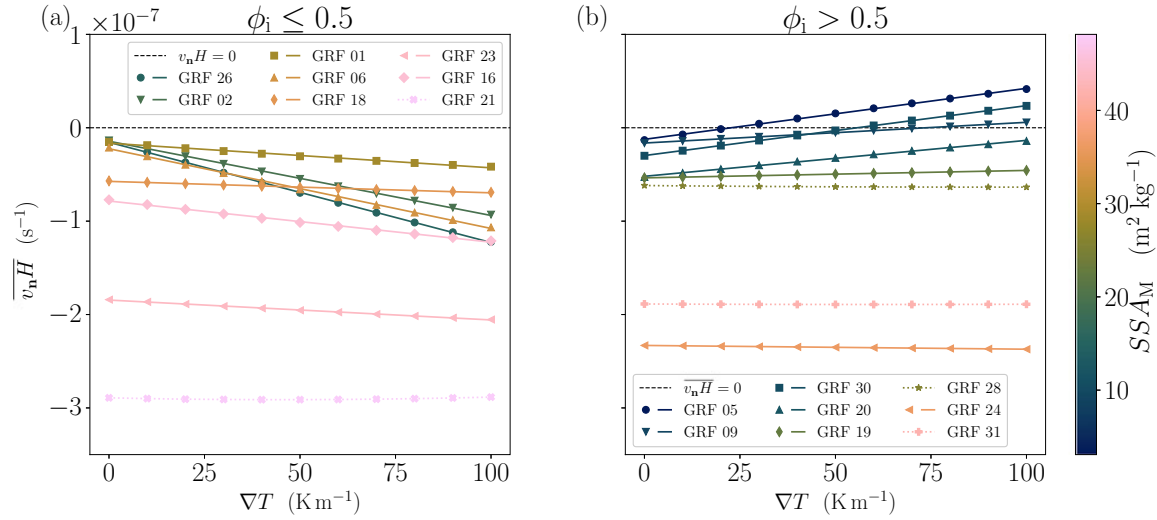
Fig. 6. Dependence of the growth rate $\overline{v_{\mathbf{n}}H}$ on ∇T for low-solid-fraction GRF microstructures on the left and high-solid-fraction microstructures on the right. Values obtained from FEM simulation are shown by markers and a linear fit by solid lines. Dotted lines indicate the non-linear (and almost constant) behaviour on a few microstructures. The colors correspond to the SSA of the samples.

growth rate on $\rho_{\mathrm{v,s}}$ is confirmed by isothermal simulations, performed at various average temperatures and everything else left the same. The simulation results are shown for two microstructures in Fig. 7a. In general, the derived linear relation is valid regardless of microstructure.

A similar analysis can be performed for the TG case. Here, the vapor fluxes are driven by fluctuations in the temperature field. As seen in the analysis on ∇T, the interface velocity $v_{\mathbf{n}}$ is proportional to β. Therefore, $v_{\mathbf{n}}$ and the growth rate $\overline{v_{\mathbf{n}}H}$ depend on the average temperature through β. This is confirmed by TG simulations ($\nabla T = 55\,\mathrm{K\,m^{-1}}$) with varied β and everything else left the same. Figure 7b shows that $\overline{v_{\mathbf{n}}H}$ is proportional to β in these TG simulations.

Surface kinetics and diffusion effects

Other important controls on the water vapor movement in snow, and thus on the SSA evolution, are the surface reactivity, which we describe as $\alpha\,v_{\mathrm{vkin}}$ and the diffusivity of water vapor D_{v}. Together, they control the transition between kinetics-limited (KL) and diffusion-limited (DL) growth. Yet, despite its importance for snow physics, the condensation coefficient α remains poorly characterized due to its measurement difficulty. It may well be that our description of surface kinetics is too simplified and that future work needs to investigate the dependence of attachment and detachment kinetics for different crystal surfaces. In
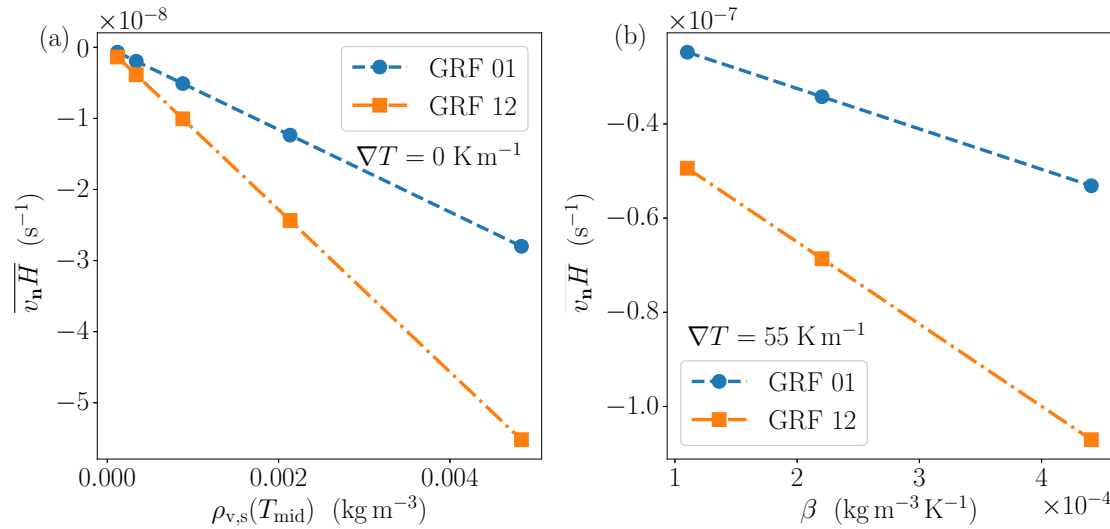
Fig. 7. (a) Growth rate $\overline{v_{\mathbf{n}}H}$ against the saturated vapor concentration $\rho_{\mathrm{v,s}}(T_{\mathrm{mid}})$ in the isothermal case, for T_{mid} ranging between 230 and 273 K. (b) Growth rate $\overline{v_{\mathbf{n}}H}$ against the derivative of saturated vapor concentration β in the TG case.

our simulations, we chose to investigate a wide range of bulk (spatially constant) condensation coefficients, ranging from 10^{-6} (typically in the kinetics-limited regime) to 10^2 (diffusion-limited regime). To probe the role of α and the KL to DL transition, we set $d_0 = 10^{-9}$ m, $T_{\mathrm{mid}} = 265.55$ K, and $\nabla T = 55$ K m^{-1}. Simulated $\overline{v_{\mathrm{n}}H}$ are displayed in Fig. 8a as a function of α. For all GRFs, the growth rate $\overline{v_{\mathrm{n}}H}$ appears to vanish for vanishing α. The vanishing α physically corresponds to an inert snow surface, onto which no deposition nor sublimation occurs. In this extreme case, no snow metamorphism happens, and the growth rate is null. In another extreme case, for high α, the growth rate reaches a plateau. Attaining a specific level is consistent with DL growth, under which the diffusion of vapor (i.e., D_{v}) in the pores is the limiting factor, and the reactivity of the interface does not further control the deposition/sublimation of water vapor (Lifshitz and Slyozov, 1961). We note that in Fig. 8 this plateau is not visible for some microstructures, either because the curve lies outside the graph (e.g. GRFs 15, 17, 21) or because the plateau appears not be fully reached for a value of $\alpha = 10^{-2}$ (e.g. GRFs 06 or 12). There is a smooth transition between these cases with clear microstructure differences. Some microstructures (e.g., GRF 12, 17, and 21 in Fig. 8) demonstrate a monotonous transition between the KL and DL regimes. Others (e.g., GRF 05, 15, and 19 in Fig. 8) disclose a non-monotonous transition, with an intermediate regime of SSA-increase between the KL and DL regimes. This non-monotonous behavior appears to be only present in sufficiently dense microstructures. This SSA growth behavior might be related to Mullins-Sekerka instabilities (Mullins and

Sekerka, 1964), i.e., tips growing faster than dips in a surrounding vapor field. However, as this phenomenon mainly appears for dense microstructures ($\phi_i > 0.5$), it is likely irrelevant for natural snow.

Braun and others (2024b) analyzed the idealized case of a sphere growing in a surrounding vapor field and proposed an analytical formula that includes the dependence to α, v_{kin}, and D_v. It has the same overall shape as the lighter samples of Fig. 8a, i.e., a monotonous decrease of $\overline{v_n H}$ with increasing alpha, with a vanishing growth rate for $\alpha = 0$ and a plateau for large α. Following the analytical sphere formula of Braun and others (2024b), we propose to model the transition from the KL to the DL regimes as

$$\frac{a_0 D_v}{1 + \frac{D_v}{\alpha \, v_{\text{kin}} \, a_1}} \tag{13}$$

where a_0 and a_1 are two free parameters (microstructure-dependent). The formula fits the notions of the KL and DL case: it is proportional to α for small α and to the diffusion coefficient D_v for large α. Moreover, the non-dimensional second Damköhler number $Da = \alpha \, v_{\text{kin}} a_1 / D_v$ arises as the control between the KL ($Da << 1$) and DL ($Da >> 1$) regimes. The essential role of the second Damköhler number is emphasized in studies that characterize the relative dynamics of the diffusion and surface kinetics processes (e.g., Bourbatache and others, 2020). We note that by design, this formula can only predict a monotonous transition between the KL and DL regimes.

Figure 8a shows the fit of Eq. (13) on a few microstructures and reveals a good agreement between Eq. (13) and the simulations. It is remarkable that the proposed formula (which is monotonous and SSA-increasing by construction) can also be roughly applied to the GRF microstructures with a non-monotonous transition between the KL and DL regimes, if the SSA-increase part is discarded.

Curvature effects

Finally, we focus on the influence of the capillary length d_0, which encodes the sensitivity to curvature fluctuations. The capillary length parameter plays a crucial role in the case of isothermal metamorphism, in which the vapor movements are driven by curvature differences (Krol and Löwe, 2016). Following the argument advanced for the study of the influence of T_{mid} in the isothermal case, the fluctuations of the saturated vapor concentration (driving the interface velocity) are proportional to $\rho_{v,s}(T_{\text{mid}})d_0 H$, i.e., proportional to the capillary length d_0. Numerical simulations performed under isothermal conditions confirm the proportionality between the growth rate and d_0 in the isothermal case. The isothermal case is well-studied, and we concentrate only on TG simulations for brevity.
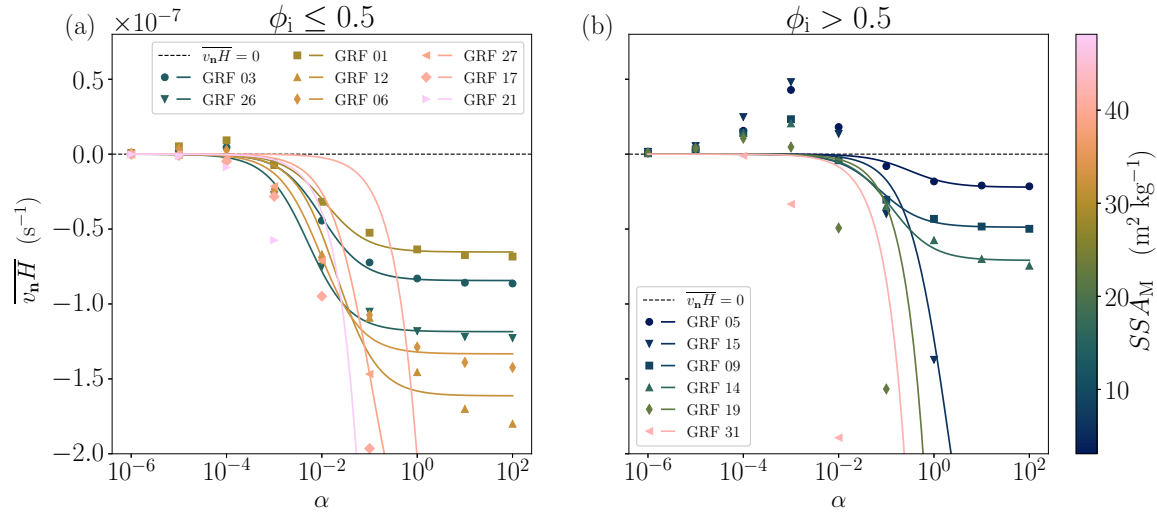
Fig. 8. Impact of the condensation coefficient α on the growth rate $\overline{v_\mathbf{n}H}$ for the GRF microstructures. Markers correspond to the results from the FEM simulations and dashed lines correspond to fits based on Eq. (13). Note that for some GRF, the DL plateau is out of the y-axis range.

The TG metamorphism case is more problematic, as the simple analysis carried out so far is no longer possible. The spatial pattern of saturated vapor is no longer proportional to d_0, as it modifies its shape due to the interaction between the curvature and temperature fluctuations. Hence, to study the influence of d_0 in the TG case, we rely on the numerical simulations (performed with $T_{\mathrm{mid}} = 265.55\,\mathrm{K}$, $\nabla T = 55\,\mathrm{K m^{-1}}$, and $\alpha = 10^{-2}$). The results of the numerical simulations, displayed in Fig. 9, indicate that the linear dependence to d_0 holds in the TG case. Moreover, all GRFs indicate a trend towards coarsening with increasing d_0. The coarsening trend is in accordance with the capillary length control over the curvature effect's magnitude. The curvature effect redistributes mass from the areas of high curvature towards low curvatures, which favors the coarsening of the microstructure. Microstructures with high SSA (especially GRFs 21-25) are more sensitive to the influence of curvature effects since they have more curvature fluctuations.

An equation for snow coarsening applicable in snowpack models

The general form of growth rate equation

The previous section revealed some specific features of the coarsening process under both isothermal and TG metamorphism. Namely, the role of temperature T_{mid} on $\rho_{\mathrm{v,s}}$ and β during isothermal and TG conditions, the linear dependence on ∇T and d_0, and the overall shape of the KL to DL transition. Based on those results, we search for a macroscopic formula to model the coarsening process, considering the influence
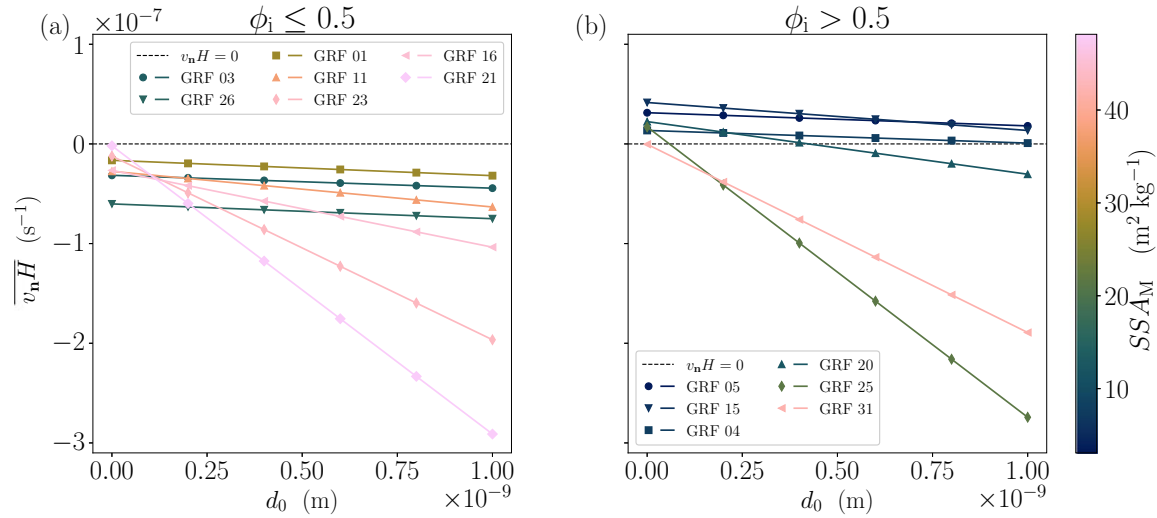
Fig. 9. Impact of the capillary length d_0 on the growth rate $\overline{v_{\mathrm{n}}H}$ for the GRF ensemble.

above of T_{mid}, ∇T, α, etc. This formula is meant to apply directly at the macroscopic level, i.e., it only involves quantities well-defined at the scale of a snow layer. This last point is necessary for use in (macroscopic) snowpack models.

As the equation governing the growth rate, we propose:

$$\overline{v_{\mathrm{n}}H} = -\frac{\frac{D_{\mathrm{v}}}{\rho_{\mathrm{i}}}\left(A(\mu)\,\beta\,\nabla T + B(\mu)\,\rho_{\mathrm{v,s}}\,d_0\right)}{1 + \frac{D_{\mathrm{v}}}{\alpha\,v_{\mathrm{kin}}\,L(\mu)}} \tag{14}$$

i.e., in terms of SSA

$$\dot{s} = 2s\overline{v_{\mathrm{n}}H} = -2s\frac{\frac{D_{\mathrm{v}}}{\rho_{\mathrm{i}}}\left(A(\mu)\,\beta\,\nabla T + B(\mu)\,\rho_{\mathrm{v,s}}\,d_0\right)}{1 + \frac{D_{\mathrm{v}}}{\alpha\,v_{\mathrm{kin}}\,L(\mu)}} \tag{15}$$

where A, B and L are free parameters that depend on the microstructure μ. The form of Eq. (14) supposes that the growth rate is the sum of a TG contribution ($\frac{D_{\mathrm{v}}}{\rho_{\mathrm{i}}}A(\mu)\,\beta\,\nabla T$) and an isothermal contribution ($\frac{D_{\mathrm{v}}}{\rho_{\mathrm{i}}}B(\mu)\,\rho_{\mathrm{v,s}}d_0$), and that both are controlled by a similar KL to DL transition ($\frac{1}{1+\frac{D_{\mathrm{v}}}{\alpha\,v_{\mathrm{kin}}\,L(\mu)}}$).

The equation offers a direct interpretation of the three parameters A, B, and L. A (expressed in m^{-1}) encodes the sensitivity of the microstructure towards TG coarsening, B (expressed in m^{-3}) encodes the sensitivity of the microstructure towards isothermal coarsening, and L (expressed in m) is a length, controlling the transition from KL to DL coarsening. Based on the interpretation of the Damköhler number $Da = \alpha\,v_{\mathrm{kin}}\,L/D_{\mathrm{v}}$ (Bourbatache and others, 2020), L should scale with the characteristic length at which the water vapor diffusion process occurs. In that sense, A, B, and L can be viewed as the material properties that govern the coarsening process, just as thermal conductivity is the material property that

governs the heat conduction process. By construction, the proposed governing equation for the growth rate can only predict coarsening (with A, B, and L positive) and, therefore, does not capture the increase in SSA observed in dense microstructures at the transition between the kinetics-limited and diffusion-limited regimes. Moreover, Eq. (14) directly sums the contribution of the curvature and TG growth rates, neglecting a potential interaction between the two. Under TG conditions, we thus expect our formula to best work in situations where the curvature effects are overridden by the TG, which could be facilitated with microstructures having a low sensitivity to isothermal metamorphism (typically low SSA microstructures) and/or a high sensitivity to TG metamorphism.

We evaluated the ability of Eq. (14) to reproduce the coarsening of low-ice-volume microstructures by comparing them with FEM results. For that, we computed random simulations (varying α, d_0, ∇T and T), and adjusted the parameters A, B and L for each microstructure with $\phi_i \leqslant 0.5$. Regarding A, B, and L as material properties, we have imposed them to be positive. For each microstructure, we validated the adjustment using a cross-validation technique. The data set was randomly split into a training set (used to adjust the parameters A, B, and L) and a test set containing 50% of the original data set. The splitting was repeated 500 times. The performance of the parametrization was assessed by the median of the adjusted coefficient of determination $\bar{R}^2$. A unique set of A, B, and L computed as the median over splits of found optimal parameters characterizes each microstructure. Figure 10 shows the results of statistical validation for each single microstructure with $\phi_i \leqslant 0$. For each evaluated microstructure, the parametrization performs very well: optimal sets of $A(\mu)$, $B(\mu)$ and $L(\mu)$ were found with $\bar{R}^2 \geqslant 0.95$ for all GRF microstructures except for GRF 17 and 18 with $\bar{R}^2 = 0.83$ and 0.86, respectively. The poorer performance of Eq. (14) on GRFs 17 and 18 indicates that its simple form is not able to fully capture the diversity of growth rates predicted by the FEM simulations. As we have a deeper understanding of the dependency of the growth rate on β, $\rho_{v,s}$, d_0, and ∇T, our intuition is that the short-coming of Eq. (14) likely stems from the assumed α dependency, which might be inadequate. For the evaluated microstructures, ϕ_i, the structural properties, the range of simulated growth rate, and the found values of A, B and L are given in Table 1. Finally, we recall that the growth rate $\overline{v_n H}$ in Figure 10 can directly be translated as the rate of change of s, using $\dot{s} = 2s\overline{v_n H}$.
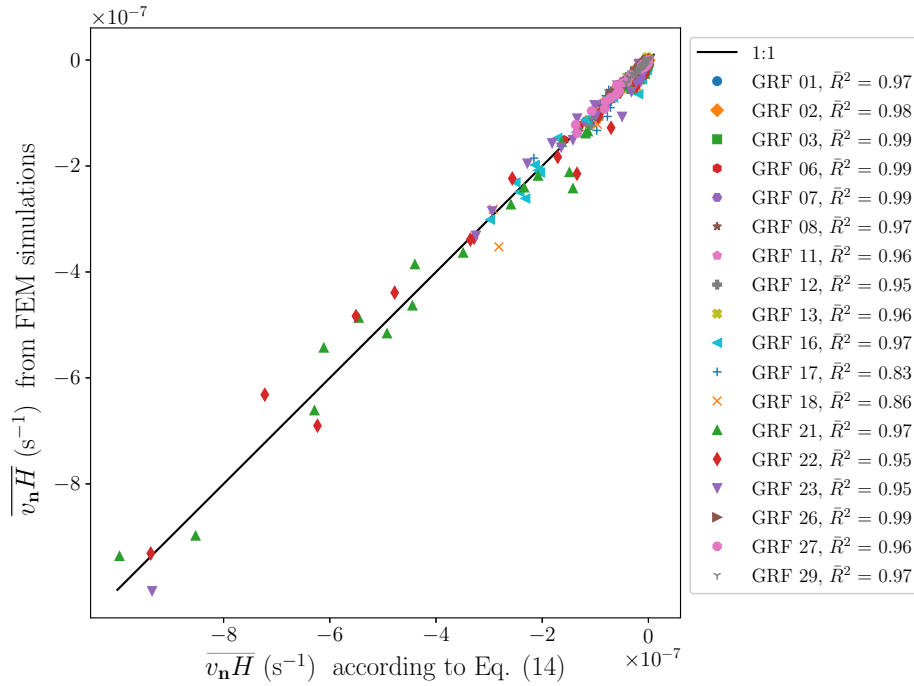
Fig. 10. Agreement between the normalized growth rate $\widehat{\overline{v_{\mathbf{n}}H}}$ obtained from FEM simulations and computed according to the parameter form (Eq. (14)) on single microstructures.

Parametrization of A, B, and L for GRF microstructures

The proposed equation Eq. (14), which governs the coarsening of snow, introduces three new material properties, namely A, B, and L. As stated above, these material properties are direct functions of the microstructure and can be estimated for each microstructure using numerical simulations performed at the pore scale. However, for Eq. (14) to be applicable in snowpack models, the material properties require to be parametrized in terms of microstructural descriptors accessible in models (just like for instance, the snow thermal conductivity is usually parametrized in terms of density for its use in snowpack models). In this section, we thus explore how A, B, and L could be parametrized.

We start with L, as it is easily interpretable. As explained above, L is akin to the length over which the diffusion process takes place. It should thus scale roughly with the pore size. Therefore, we propose to express L as a function of $1/s$. Figure 11 displays a scatter plot of the previously found L values as a function of $1/s$. Despite some scatter, it appears that L is linearly related to $1/s$ and can be parameterized as a_{L}/s (a_{L} being a free parameter to be fitted).

For the parameter B, we exploit that it governs the sensitivity to curvature effects and isothermal metamorphism. It is thus expected to be high in microstructures characterized by sharp variations of the

local curvature. Following Krol and Löwe (2016), we thus search B as a function of the standard deviation of the curvature $\sigma_H = \overline{H^2} - \overline{H}^2$. As displayed in Fig. 11, B relate linearly to $\sigma_H^{1.5}$ quite well. The exponent 1.5 ensures the dimensional consistency between B and σ_H. Thus, we search B as $B = a_B \sigma_H^{1.5}$ with a_B to be fitted. Finally, the parameterization of A revealed itself to be more problematic. In their analysis of snow coarsening under TG, Flanner and Zender (2006) proposed that the sensitivity towards TG is related to the fluctuations in inter-granular spacing in snow. While the analysis considers snow as an ensemble of disconnected ice spheres rather than a bi-continuous microstructure, it makes intuitive sense that coarsening under TG conditions is related to the ability of some portions of the microstructure to preferentially attract vapor due to their favored position compared to other portions. Furthermore, Flanner and Zender (2006) proposed that the fluctuations in inter-granular spacing scale with the inter-granular spacing itself. In a regular array of spheres, this inter-granular spacing GS is defined as

$$\mathrm{GS} = \left(\frac{4\pi\phi_i}{s^3\,\phi_i}\right)^{1/3} - \frac{2\phi_i}{s} \tag{16}$$

However, in the case of the GRF microstructures, we found that using GS alone is a poor predictor of A, leading to a large scatter. Motivated by the dimension of A (m^{-1}), we found instead a weak correlation between A and s/ϕ_i, as seen in Fig. 11. No significantly better correlation was found with other simple microstructural descriptors. Thus, in the lack of a better parametrization, we take A as a constant a_A to be adjusted.

Despite the correlations found for the predictions of B and L, some scatter remains, as visible in the three panels of Fig. 11. Hence, the parameterizations proposed in this section are only a preliminary attempt and should be refined to capture better the impact of the microstructure on the coarsening process. Notably, the use of other microstructural descriptors in the parameterization should be considered. As discussed below, it also remains to evaluate how these parameterizations translate for actual snow microstructures.

A parametrized equation for microstructure coarsening

Based on the parametrizations discussed above, we thus propose the following equation to model the growth rate of a microstructure:

$$\overline{v_n H} = -\frac{\frac{D_v}{\rho_i}\left(a_A\beta\nabla T + a_B\sigma_H^{1.5}\rho_{v,s}d_0\right)}{1 + \frac{D_v}{\alpha v_{kin}a_L/s}} \tag{17}$$
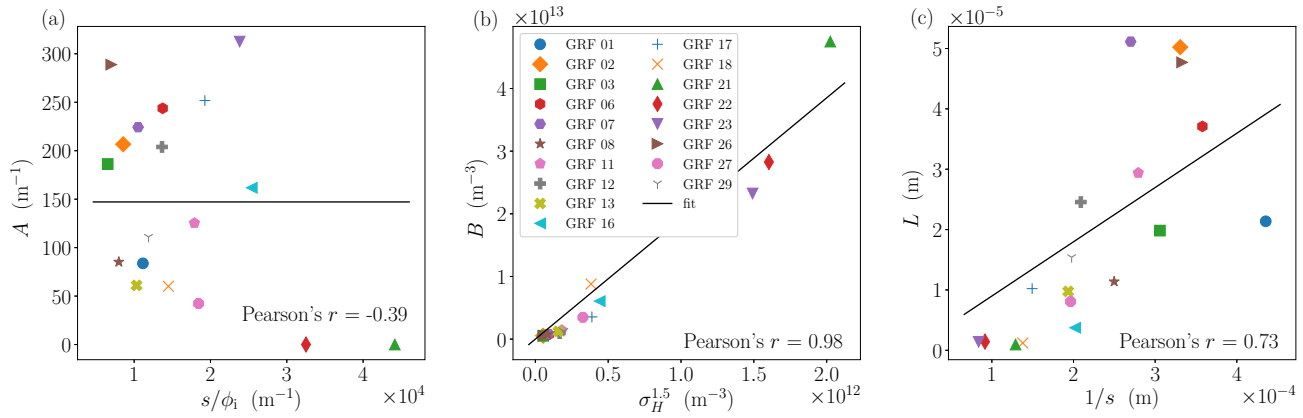
Fig. 11. Prediction of A, B, and L as functions of the microstructural descriptors. (a) A as a function of s/ϕ_i with a constant fit. (b) B as a function of $\sigma_H^{1.5}$ with a linear fit. (c) L as a function of $1/s$ with a linear fit.

i.e., in terms of SSA

$$\dot{s} = 2\,s\,\overline{v_{\mathbf{n}}H} = -2\,s\,\frac{\frac{D_v}{\rho_i}\left(a_A\,\beta\,\nabla T + a_B\,\sigma_H^{1.5}\,\rho_{v,s}\,d_0\right)}{1 + \frac{D_v}{\alpha\,v_{kin}\,a_L/s}} \tag{18}$$

where a_A, a_B, and a_L are three free parameters to be adjusted. We stress that these three parameters are meant to apply for all the GRF microstructures with $\phi_i \leqslant 0.5$. To adjust these parameters and assess the ability of Eq. (17) to predict the growth rate of a range of microstructures, we employ the same cross-validation technique as used above. The resulting values are $a_A = 134.8\,\mathrm{m}^{-1}$, $a_B = 19.0$, and $a_L = 1.13 \times 10^{-2}$ with a median $\bar{R}^2$ of 0.95 and $[0.90, 0.96]$ as the 95 % confidence interval. The results are visualized for the median of free parameters in Fig. 12. As seen in the figure, the scatter is more marked than in Fig. 10. The reason for this is that the reduction of the total number of free parameters (from three per microstructure to only three in total), which results in a degradation of the prediction of the material properties A, B, and L. This problem is especially marked for A that varies substantially for different microstructures and that encodes the critical dependence to TG metamorphism. Nonetheless, we have obtained a governing law for the growth rate with only three free parameters that reasonably reproduces the simulated growth rate for various conditions (T_{mid}, ∇T, α, etc.) and microstructures.

A first application to snow

Here, we briefly evaluate the ability of the proposed law and parametrization to model the coarsening of actual snow samples. For this, we rely on the experimental data obtained by Pinzer and others (2012) under controlled TG conditions. The experimental data consist of a time series of μCT images, regularly performed during a $\sim 400\,\mathrm{h}$ long experiment under a TG of $47\,\mathrm{K\,m}^{-1}$ and an average temperature of
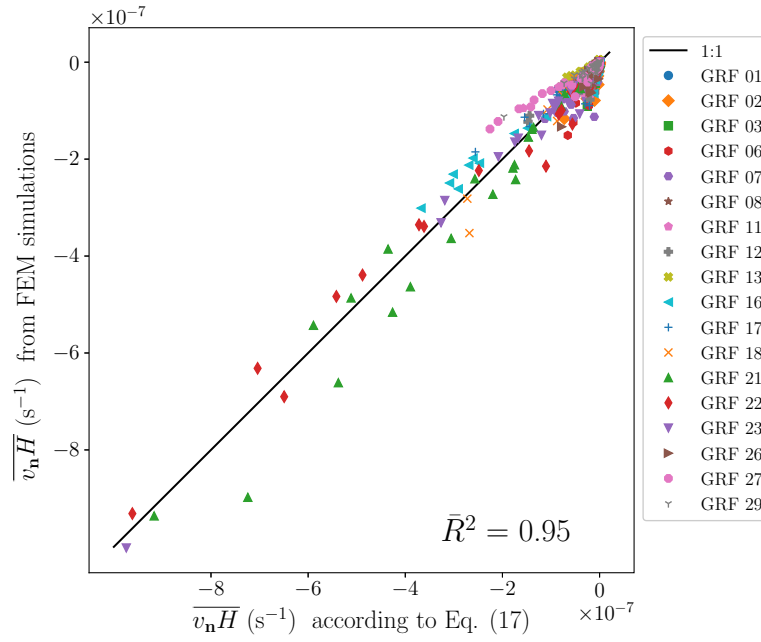
Fig. 12. Evaluation of the growth rate $\overline{v_{\mathbf{n}} H}$ obtained from Eq. (17) against the FEM simulations on multiple microstructures.

$-8.1\,^\circ\text{C}$. The experimental growth rate $\overline{v_{\mathbf{n}} H}$ at the ith time step can be derived as:

$$\overline{v_{\mathbf{n}} H} = \frac{\dot{s}}{2\,s} \simeq \frac{s^{i+1} - s^i}{2\,s^i\,\Delta t} \tag{19}$$

where Δt is the time step between two consecutive images.

Moreover, the μCT images provide the necessary microstructural descriptors to apply our proposed growth rate equation with the GRF-based parametrization of A, B, and L. For the value of α in the growth rate equation, we follow the work of Braun and others (2024b) that found a shift from 10^{-1} to $10^{-1.5}$ around the middle of the experiment. This decrease of the α under TG conditions has been interpreted as a result of the development of facets. The capillary length is taken as $d_0 = 10^{-9}\,\text{m}$ (Kaempfer and Plapp, 2009).

A comparison between the experimental and modeled growth rates is displayed in panel a of Fig. 13. The translation of the growth rates in terms of an SSA time series is displayed alongside in panel b. We note that in the case of the SSA time series, errors on growth rate accumulate over time, potentially leading to a large error at the end of the time series. The transition in α is visible as a sharp drop of the growth rate around the 160 h, both in the modeled and experimental values. The direct application of the growth rate equation with the GRF-based parametrization yields a very good agreement with the
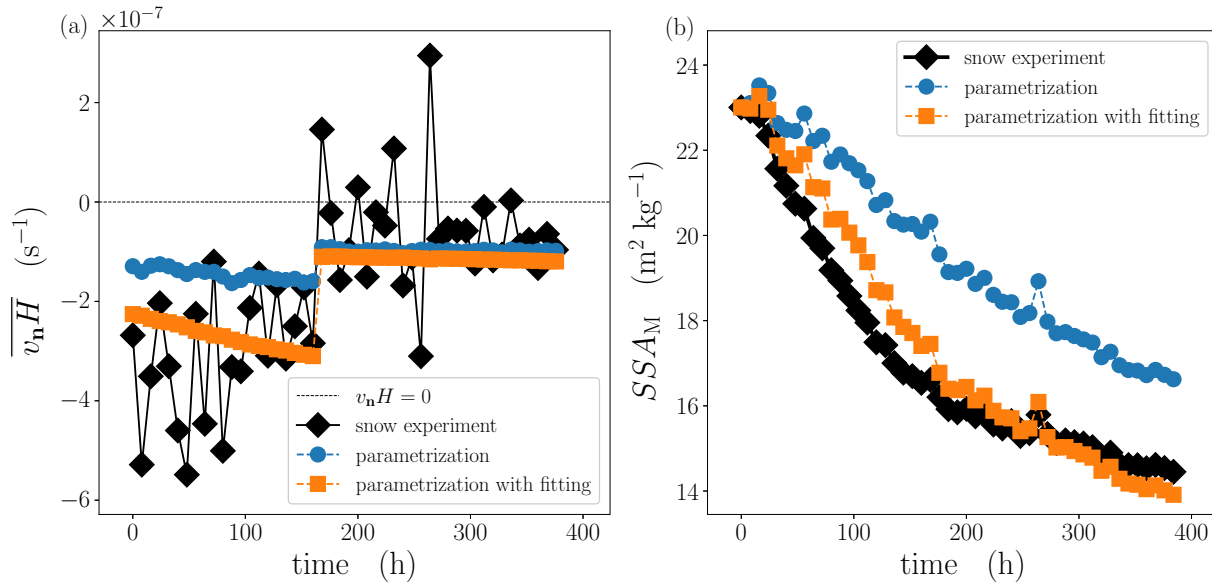
Fig. 13. Evaluation of the proposed parametrization against experimental observations of snow metamorphism. (a) Comparison between observed growth rates (black) and predicted growth rates using Eq.17 (blue and orange). (b) Comparison between observed SSA values (black) and the predicted SSA time series integrating Eq. 18 over time (blue and orange).

experiment in the second part of the time series, but clearly underestimate the coarsening in the first part. Our interpretation is that this likely comes from an underestimation of A, the TG sensitivity, from the GRF-based parametrization in the first portion of the experiment that might not be suitable for actual snow. Thus, we assess whether another parametrization of A, B, and L could yield a better agreement with the experimental data. For this, we kept the assumed dependence of A, B, and L on the microstructural descriptors, but re-adjusted the coefficients a_A, a_B, and a_L of Eq. (17) on the experimental data. After adjustment, we obtained the optimal values $a_A = 1320\,\mathrm{m}^{-1}$, $a_B = 1.52 \times 10^{-2}$, and $a_L = 1.09 \times 10^{-2}$. This second parametrization notably yields higher TG sensitivities (A) and smaller length scales governing the KL to DL transition (L). As displayed in panel a of Fig. 13, this results in a better agreement of the growth rates over the whole experimental time series, with notably a faster coarsening in the first part (due to higher A values) and a sharper effect of the α transition (due to smaller L values). In this case, growth rate errors do not accumulate over time, leading to a good prediction of the SSA over the whole time series, as seen in panel b of Fig.13. These results suggest that when properly parametrized, the growth rate equations proposed in this article can be accurately applied to snow.

Relations to the LSW theory and previous works

Based on the theory of Lifshitz, Slyozov, and Wagner (Lifshitz and Slyozov, 1961; Wagner, 1961), Legagneux and others (2004) showed that the isothermal SSA evolution of an ensemble of dispersed spheres could be modeled as

$$s(t) = s_0 \left(\frac{\tau}{t + \tau} \right)^{1/n} \tag{20}$$

with s_0 the initial SSA, τ a characteristic time which is a function of the initial SSA and the physics at play, and n an exponent equal to 3 in the DL case and 2 in the KL case. While the formula was derived assuming an ensemble sphere, it has been successfully applied to snow. One can thus wonder how the framework proposed in this article relates to that of Lifshitz and Slyozov (1961), Wagner (1961), and Legagneux and others (2004), and if they can be reconciled.

First, we recall that we have assumed above that B could be assumed as proportional to $\sigma_H^{1,5}$. We have chosen σ_H as the predictor, as isothermal metamorphism is driven by curvature fluctuations. However, curvature fluctuations are also closely related to the SSA. Indeed, dimensional analysis suggests that σ_H scales with s^2. This is confirmed by our GRF ensemble, which reveals a linear relation between σ_H and s^2/ϕ_i^2 (not shown). Therefore, a potential parametrization could also be of the form $B \propto s^3$.

We now analyze the DL case ($D_a >> 1$). Here, Eq. (15) simplifies to $\dot{s} = -2s \frac{D_v}{\rho_i} \rho_{v,s} d_0 B(\mu)$. Taking $B \propto s^3$, we obtain that $\dot{s} \propto -s^4$. The solution of such differential equation has the form $s = s_0 \left(\frac{\tau}{t+\tau} \right)^{1/3}$. This directly corresponds to the form proposed by Legagneux and others (2004). Similarly, in the KL case ($D_a << 1$), Eq. (15) simplifies to $\dot{s} = -2s \frac{\rho_{v,s}}{\rho_i} d_0 \alpha v_{kin} L(\mu) B(\mu)$. With $L \propto s^{-1}$, we have that $\dot{s} \propto -s^3$. The solution of this differential equation is $s = s_0 \left(\frac{\tau}{t+\tau} \right)^{1/2}$. Again, this matches the result of Legagneux and others (2004) for the DL case.

Current limitations and future work

We expect Eq. (14) to apply for a large range of microstructures (under the restriction that $\phi_i \leqslant 0.5$), as it is informed by the general physics governing deposition and sublimation at the pore-scale. Yet, the parametrization of the material properties A, B, and L revealed itself to be more problematic. The difficulty of finding an accurate parametrization for many microstructures results in the spread of Fig. 12.

This is especially due to the difficult parametrization of A, which cannot easily be related to descriptors of the microstructure. Further work should therefore be dedicated to investigating its microstructural

drivers, i.e. why different microstructures coarsen differently under TG conditions, in an effort to derive a more accurate parametrization. The simplified description of surface kinetics via a spatially and temporally constant factor α can play a role here.

Moreover, the parametrization proposed here for B involves the quantity $\overline{H^2}$. While this is a well-defined macroscopic quantity, it is usually not included in snowpack modeling. Indeed, models are usually restricted to the ice volume fraction (given by density) and the surface specific area (grain size or optical diameter) in terms of objective descriptors of the microstructure. The use of quantities such as $\overline{H^2}$ would thus require to introduce its governing equation, in order to properly close the system of equations. Fortunately, an upscaled equation for $\overline{H^2}$ is provided in (Krol and Löwe, 2018). As with the upscaled SSA equation, it involves the interface velocity and the local curvatures, averaged over the ice-air interface of the sample. Translating this equation in terms of macroscopic quantities (density, SSA, etc.) would require a similar treatment as done in this article for the upscaled SSA equation.

In order to avoid the use of $\overline{H^2}$, we note that it could be possible to rather use a parametrization in terms of s and ϕ_i. While we obtain reasonable results using s/ϕ_i as a predictor for B, we think that this was helped by the fact that the GRF microstructures share a similar morphology (i.e., the "grains" all resemble rounded grains in the snow classification). The different microstructures can thus be seen as spatially scaled versions of one another: a fine microstructure with a large SSA corresponds to a larger microstructure that would have been spatially shrunk. In this condition, a direct relation between s^2/ϕ_i^2 and $\overline{H^2}$ can be expected. However, we do not know if such a relation would hold in the case of microstructures with different morphologies (i.e., different snow types).

Following this last point, a limitation of the work presented here is that, while the use of GRF allows us to precisely control the porosity and SSA of the microstructures, it does not have the variability of natural snow in terms of morphologies. Further work should be dedicated to extend this study to actual snow samples, measured under μCT and to investigate the quantitative differences between morphologies (i.e., Facetted Crystals, Depth Hoar, Precipitation Particles, etc. Fierz and others, 2009) during coarsening under both isothermal and TG conditions.

Finally, we recall that our study did not consider the role of mechanical deformation on the SSA evolution. One reason for this is that the mechanism(s) driving the plastic deformation of snow at the pore-scale remains unknown (Fourteau and others, 2024) and therefore cannot be implemented in our

FEM simulations. Yet, we expect that neglecting the ice matrix deformation is not a strongly limiting assumption of this work. Indeed, while the theoretical Eq. (15) of Krol and Löwe (2018) indicates that the deformation of the ice matrix can have an influence on the SSA, the experimental study of Schleef and Loewe (2013) did not observe any impact of the densification on the SSA of light snow samples. The use of pore-scale simulations could be a tool to investigate the relative contribution and interactions of metamorphism and deformation on the SSA evolution. But this will first require an understanding of the mechanism(s) driving the deformation of the ice matrix.

CONCLUSIONS

In this work, we combined the pore-scale physics governing the deposition and sublimation of water vapor and the upscaled geometrical equation of Krol and Löwe (2018) to quantify the rate of change of SSA in various microstructures. For that, we set up the FEM simulations of the water vapor in snow and its deposition/sublimation at the ice-air interface, from which the rate of change of SSA can be assessed. The simulations were performed on artificially generated microstructures, which allows us to precisely control the ice volume fraction and SSA of the microstructures. Despite being artificially generated, these microstructures resemble typical rounded grains of snow at low density and polar firn at higher densities. By working directly with bi-continuous matrices of ice and air, this study does not need to consider snow as an ensemble of spheres, offering a more realistic view of the material.

The simulation revealed a contrasted behavior between low density ($\phi_i \leqslant 0.5$) and high density ($\phi_i > 0.5$) microstructures, that we interpret as a difference between convex and concave microstructures. In some conditions, the simulations revealed the possibility of SSA increase, likely related to Mullins-Sekerka interface instabilities.

Based on simple physical arguments, we derive a law governing the coarsening of the microstructures with $\phi_i \leqslant 0.5$. This law is meant to be applied under various ambient conditions, isothermal or under a TG. The law explicitly takes into account the influence of the physical parameters controlling the pore-scale processes, namely the diffusion coefficient of vapor in air, the kinetics of surface deposition/sublimation (i.e. the condensation coefficient of water vapor onto ice and the so-called kinetics velocity), and the capillary length. This formula introduces 3 material properties that fully characterize the coarsening of the microstructures. These material properties directly and solely depend on the microstructure. These coefficients correspond to the sensitivity of the microstructures to coarsening under TG conditions, the

sensitivity of the microstructure to coarsening under isothermal conditions, and the length scale controlling the transition from kinetics-limited to diffusion-limited regimes.

The ability of the proposed formula to capture the coarsening of various microstructures has been verified using the pore-scale FEM simulations ($R \gtrapprox 0.95$). Using these simulations, we then investigate the relation between the 3 new material properties and the microstructure, with the goal of deriving a parametrization applicable in snowpack models. We were able to derive parametrizations for the sensitivity of the microstructure to coarsening under isothermal conditions and the kinetics-limited to diffusion-limited length scale, based on the SSA and the second moment of the curvature distribution. However, the parametrization of the sensitivity of the microstructure to coarsening under TG conditions remains evasive, as no clear link with a simple descriptor of the microstructure was observed. Nonetheless, once parametrized in terms of microstructural descriptors, we were able to reasonably predict the coarsening rate of various snow-like microstructures ($R \approx 0.95$). Finally, we evaluated the ability of the proposed law to predict experimental snow coarsening data. Direct application of the GRF-based parametrization resulted in an underestimation of the growth rate, but results could be significantly improved by adjusting the TG sensitivity and length scale parametrization.

We believe the approach in this article benefits our comprehension of snow coarsening and its representation in models. Setting a physically based governing law, reduces the complexity of the coarsening process to only three material properties that can be estimated from numerical simulations and/or controlled experiments and are directly interpretable. A similar approach could also be used to derive the equation governing the evolution of the curvature and its moment, should it be necessary to close the system of equations describing the evolution of the snow material over time.

APPENDIX

DATA

We published simulation parameters and outputs for this study on the data portal EnviDat, https://doi.org/10.16904/envidat.569 (Braun and others, 2024a).

structure	ϕ_i	$SSA_M(\text{kg m}^{-2})$	# of sim.	$\max\lvert\overline{v_\mathbf{n}H}\rvert$	median $\bar{R}^2$	median A	median B	median L
GRF 01	0.21	12.2	57	$5.57{\cdot}10^{-8}$	0.97	$8.38{\cdot}10^1$	$6.38{\cdot}10^{11}$	$2.14{\cdot}10^{-5}$
GRF 02	0.35	9.3	43	$1.16{\cdot}10^{-7}$	0.98	$2.07{\cdot}10^2$	$5.42{\cdot}10^{11}$	$5.02{\cdot}10^{-5}$
GRF 03	0.50	7.1	57	$9.07{\cdot}10^{-8}$	0.99	$1.86{\cdot}10^2$	$5.31{\cdot}10^{11}$	$1.98{\cdot}10^{-5}$
GRF 06	0.20	15.0	47	$1.51{\cdot}10^{-7}$	0.99	$2.44{\cdot}10^2$	$7.26{\cdot}10^{11}$	$3.71{\cdot}10^{-5}$
GRF 07	0.35	11.5	57	$1.17{\cdot}10^{-7}$	0.99	$2.24{\cdot}10^2$	$8.05{\cdot}10^{11}$	$5.11{\cdot}10^{-5}$
GRF 08	0.50	8.7	43	$5.20{\cdot}10^{-8}$	0.97	$8.52{\cdot}10^1$	$7.62{\cdot}10^{11}$	$1.14{\cdot}10^{-5}$
GRF 11	0.20	19.5	47	$9.49{\cdot}10^{-8}$	0.96	$1.25{\cdot}10^2$	$1.43{\cdot}10^{12}$	$2.94{\cdot}10^{-5}$
GRF 12	0.35	14.9	43	$1.23{\cdot}10^{-7}$	0.95	$2.04{\cdot}10^2$	$9.57{\cdot}10^{11}$	$2.46{\cdot}10^{-5}$
GRF 13	0.50	11.3	47	$6.26{\cdot}10^{-8}$	0.96	$6.10{\cdot}10^1$	$1.23{\cdot}10^{12}$	$9.75{\cdot}10^{-6}$
GRF 16	0.19	27.7	57	$3.01{\cdot}10^{-7}$	0.97	$1.62{\cdot}10^2$	$6.07{\cdot}10^{12}$	$3.73{\cdot}10^{-6}$
GRF 17	0.35	21.0	47	$1.85{\cdot}10^{-7}$	0.83	$2.52{\cdot}10^2$	$3.53{\cdot}10^{12}$	$1.02{\cdot}10^{-5}$
GRF 18	0.50	15.8	43	$3.53{\cdot}10^{-7}$	0.86	$6.01{\cdot}10^1$	$8.79{\cdot}10^{12}$	$1.21{\cdot}10^{-6}$
GRF 21	0.18	48.2	57	$9.36{\cdot}10^{-7}$	0.97	$6.49{\cdot}10^{-17}$	$4.75{\cdot}10^{13}$	$9.52{\cdot}10^{-7}$
GRF 22	0.34	35.5	39	$9.31{\cdot}10^{-7}$	0.95	$1.13{\cdot}10^{-13}$	$2.83{\cdot}10^{13}$	$1.44{\cdot}10^{-6}$
GRF 23	0.50	26.0	50	$1.00{\cdot}10^{-6}$	0.95	$3.13{\cdot}10^2$	$2.32{\cdot}10^{13}$	$1.40{\cdot}10^{-6}$
GRF 26	0.43	7.6	57	$1.33{\cdot}10^{-7}$	0.99	$2.89{\cdot}10^2$	$5.51{\cdot}10^{11}$	$4.77{\cdot}10^{-5}$
GRF 27	0.28	20.1	39	$1.38{\cdot}10^{-7}$	0.96	$4.24{\cdot}10^1$	$3.48{\cdot}10^{11}$	$8.07{\cdot}10^{-6}$
GRF 29	0.43	13.0	60	$1.12{\cdot}10^{-7}$	0.97	$1.11{\cdot}10^2$	$1.29{\cdot}10^{11}$	$1.54{\cdot}10^{-5}$

Table 1. Overview of structural properties (ϕ_i, SSA_M), the number of random simulations (# of sim.), the maximum absolute value of the simulated growth rate $\max\lvert\overline{v_\mathbf{n}H}\rvert$ and the statistical validation results of the derived governing law (median of adjusted coefficient of determination $\bar{R}^2$ and the three introduced material properties A, B, L) for single GRF microstructures with $\phi_i \leqslant 0.5$

.

ACKNOWLEDGEMENTS

FINANCIAL SUPPORT

AUTHOR CONTRIBUTIONS

The research was designed by HL. The program used for GRF generation was developed by SF with supervision of HL. The numerical simulations were performed by AB. The interpretation of the results was performed by AB and KF with the help of ML. The manuscript was written by AB with feedbacks from all co-authors.

REFERENCES

Bartelt P and Lehning M (2002) A physical snowpack model for the swiss avalanche warning: Part i: numerical model. *Cold Regions Science and Technology*, **35**(3), 123–145 (doi: 10.1016/S0165-232X(02)00074-5)

Bear J and Bachmat Y (2012) *Introduction to modeling of transport phenomena in porous media*, volume 4. Springer Science & Business Media (doi: 10.1007/978-94-009-1926-6)

Blatny L, Löwe H, Wang S and Gaume J (2021) Computational micromechanics of porous brittle solids. *Computers and Geotechnics*, **140**, 104284, ISSN 0266-352X (doi: 10.1016/j.compgeo.2021.104284)

Blatny L, Löwe H and Gaume J (2023) Microstructural controls on the plastic consolidation of porous brittle solids. *Acta Materialia*, **250**, 118861, ISSN 1359-6454 (doi: 10.1016/j.actamat.2023.118861)

Bourbatache M, Millet O and Moyne C (2020) Upscaling diffusion–reaction in porous media. *Acta Mechanica*, **231**, 2011–2031 (doi: 10.1007/s00707-020-02631-9)

Bouvet L, Calonne N, Flin F and Geindreau C (2022) Snow equi-temperature metamorphism described by a phase-field model applicable on micro-tomographic images: Prediction of microstructural and transport properties. *Journal of Advances in Modeling Earth Systems*, **14**(9), e2022MS002998 (doi: 10.1029/2022MS002998)

Braun A, Fourteau K, Frei S, M L and Löwe H (2024a) Simulation parameters and outputs for towards a physically and microstructure-based equation for the evolution of the specific surface area in snow. *EnviDat [data set]* (doi: 10.16904/envidat.569)

Braun A, Fourteau K and Löwe H (2024b) A rigorous approach to the specific surface area evolution in snow during temperature gradient metamorphism. *The Cryosphere*, **18**(4), 1653–1668 (doi: 10.5194/tc-18-1653-2024)

Burr A, Ballot C, Lhuissier P, Martinerie P, Martin CL and Philip A (2018) Pore morphology of polar firn around closure revealed by x-ray tomography. *The Cryosphere*, **12**(7), 2481–2500 (doi: 10.5194/tc-12-2481-2018)

Calonne N, Geindreau C and Flin F (2014) Macroscopic modeling for heat and water vapor transfer in dry snow by homogenization. *The Journal of Physical Chemistry B*, **118**(47), 13393–13403 (doi: 10.1021/jp5052535)

Calonne N, Richter B, Löwe H, Cetti C, ter Schure J, Van Herwijnen A, Fierz C, Jaggi M and Schneebeli M (2020) The rhossa campaign: multi-resolution monitoring of the seasonal evolution of the structure and mechanical stability of an alpine snowpack. *The Cryosphere*, **14**(6), 1829–1848 (doi: 10.5194/tc-14-1829-2020)

Ding KH, Xu X and Tsang L (2010) Electromagnetic scattering by bicontinuous random microstructures with discrete permittivities. *IEEE Transactions on Geoscience and Remote Sensing*, **48**(8), 3139–3151 (doi: 10.1109/TGRS.2010.2043953)

Domine F, Taillandier AS, Cabanes A, Douglas T and Sturm M (2009) Three examples where the specific surface area of snow increased over time. *The Cryosphere*, **3**(1), 31–39 (doi: 10.5194/tc-3-31-2009)

Drew DA (1990) Evolution of geometric statistics. *SIAM Journal on Applied Mathematics*, **50**(3), 649–666, ISSN 00361399

Eckert N, Corona C, Giacona F, Gaume J, Mayer S, van Herwijnen A, Hagenmuller P and Stoffel M (2024) Climate change impacts on snow avalanche activity and related risks. *Nature Reviews Earth & Environment*, 1–21 (doi: 10.1038/s43017-024-00540-2)

Fierz C, Armstrong RL, Durand Y, Etchevers P, Greene E, McClung DM, Nishimura K, Satyawali PK and Sokratov SA (2009) *TheInternational Classificationi for Seasonal Snow on the Groun*. UNESCO/IHP

Flanner MG and Zender CS (2006) Linking snowpack microphysics and albedo evolution. *Journal of Geophysical Research: Atmospheres*, **111**(D12) (doi: 10.1029/2005JD006834)

Flin F and Brzoska JB (2008) The temperature-gradient metamorphism of snow: vapour diffusion model and application to tomographic images. *Annals of Glaciology*, **49**, 17–21 (doi: 10.3189/172756408787814834)

Fourteau K, Domine F and Hagenmuller P (2020) Macroscopic water vapor diffusion is not enhanced in snow. *The Cryosphere Discussions*, 1–23 (doi: 10.5194/tc-15-389-2021)

Fourteau K, Domine F and Hagenmuller P (2021a) Impact of water vapor diffusion and latent heat on the effective thermal conductivity of snow. *The Cryosphere*, **15**(6), 2739–2755 (doi: 10.5194/tc-15-2739-2021)

Fourteau K, Domine F and Hagenmuller P (2021b) Macroscopic water vapor diffusion is not enhanced in snow. *CRYOSPHERE*, **15**(1), 389–406, ISSN 1994-0416 (doi: 10.5194/tc-15-389-2021)

Fourteau K, Freitag J, Malinen M and Löwe H (2024) Microstructure-based simulations of the viscous densification of snow and firn. *The Cryosphere*, **18**(6), 2831–2846 (doi: 10.5194/tc-18-2831-2024)

Freitag J, Wilhelms F and Kipfstuhl S (2004) Microstructure-dependent densification of polar firn derived from x-ray microtomography. *Journal of Glaciology*, **50**(169), 243250 (doi: 10.3189/172756504781830123)

Grenfell T and SG W (1999) Representation of a nonspherical ice particle by a collection of independent spheres for scattering and absorption of radiation. *J. Geophys. Res. Atm.*, **104**(D24), 31697–31709 (doi: 10.1029/1999JD900496)

Guo E, Phillion A, Cai B, Shuai S, Kazantsev D, Jing T and Lee PD (2017) Dendritic evolution during coarsening of mg-zn alloys via 4d synchrotron tomography. *Acta Materialia*, **123**, 373–382 (doi: 10.1016/j.actamat.2016.10.022)

Kaempfer TU and Plapp M (2009) Phase-field modeling of dry snow metamorphism. *Physical Review E*, **79**(3), 031502 (doi: 10.1103/PhysRevE.79.031502)

Krol Q and Löwe H (2016) Analysis of local ice crystal growth in snow. *Journal of Glaciology*, **62**(232), 378–390 (doi: 10.1017/jog.2016.32)

Krol Q and Löwe H (2018) Upscaling ice crystal growth dynamics in snow: Rigorous modeling and comparison to 4d x-ray tomography data. *Acta Materialia*, **151**, 478–487 (doi: 10.1016/j.actamat.2018.03.010)

Legagneux L, Taillandier AS and Domine F (2004) Grain growth theories and the isothermal evolution of the specific surface area of snow. *Journal of applied physics*, **95**(11), 6175–6184 (doi: 10.1063/1.1710718)

Libbrecht KG (2005) The physics of snow crystals. *Reports on progress in physics*, **68**(4), 855 (doi: 10.1088/0034-4885/68/4/R03)

Libbrecht KG (2021) *Snow Crystals: A Case Study in Spontaneous Structure Formation*. Princeton University Press (doi: 10.2307/j.ctv1qdqztv)

Lifshitz IM and Slyozov VV (1961) The kinetics of precipitation from supersaturated solid solutions. *Journal of physics and chemistry of solids*, **19**(1-2), 35–50 (doi: 10.1016/0022-3697(61)90054-3)

Löwe H, Spiegel J and Schneebeli M (2011) Interfacial and structural relaxations of snow under isothermal conditions. *Journal of Glaciology*, **57**(203), 499–510 (doi: 10.3189/002214311796905569)

Malinen M and Råback P (2013) *Elmer finite element solver for multiphysics and multiscale problems*, volume 19, 101–113. Schriften des Forschungszentrums Julich, IAS Series Julich, Germany, ISBN 978-3-89336-899-0

Martin J and Schneebeli M (2023) Impact of the sampling procedure on the specific surface area of snow measurements with the icecube. *The Cryosphere*, **17**(4), 1723–1734 (doi: 10.5194/tc-17-1723-2023)

Meloche J, Langlois A, Rutter N, Royer A, King J, Walker B, Marsh P and Wilcox EJ (2022) Characterizing tundra snow sub-pixel variability to improve brightness temperature estimation in satellite swe retrievals. *The Cryosphere*, **16**(1), 87–101 (doi: 10.5194/tc-16-87-2022)

Montpetit B, Royer A, Langlois A, Cliche P, Roy A, Champollion N, Picard G, Domine F and Obbard R (2012) New shortwave infrared albedo measurements for snow specific surface area retrieval. *Journal of Glaciology*, **58**(211), 941952 (doi: 10.3189/2012JoG11J248)

Morin S, Horton S, Techel F, Bavay M, Coléou C, Fierz C, Gobiet A, Hagenmuller P, Lafaysse M, Liar M, Mitterer C, Monti F, Müller K, Olefs M, Snook JS, van Herwijnen A and Vionnet V (2020) Application of physical snowpack models in support of operational avalanche hazard forecasting: A status report on current implementations and prospects for the future. *Cold Regions Science and Technology*, **170**, 102910, ISSN 0165-232X (doi: 10.1016/j.coldregions.2019.102910)

Mott R, Winstral A, Cluzet B, Helbig N, Magnusson J, Mazzotti G, Quéno L, Schirmer M, Webster C and Jonas T (2023) Operational snow-hydrological modeling for switzerland. *Frontiers in Earth Science*, **11**, 1228158 (doi: 10.3389/feart.2023.1228158)

Moyne C, Batsale J and Degiovanni A (1988) Approche expérimentale et théorique de la conductivité thermique des milieux poreux humidesii. théorie. *Int. J. Heat Mass Transf.*, **31**(11), 2319–2330, ISSN 0017-9310 (doi: 10.1016/0017-9310(88)90163-9)

Mullins WW and Sekerka RF (1964) Stability of a Planar Interface During Solidification of a Dilute Binary Alloy. *J. Appl. Phys.*, **35**(2), 444–451 (doi: 10.1063/1.1713333)

Osório WR, Goulart PR, Santos GA, Neto CM and Garcia A (2006) Effect of dendritic arm spacing on mechanical properties and corrosion resistance of al 9 wt pct si and zn 27 wt pct al alloys. *Metallurgical and Materials Transactions A: Physical Metallurgy and Materials Science*, **37**(8), 2525 2538 (doi: 10.1007/BF02586225)

P R Goulart JES W R Osório and Garcia A (2007) Dendritic microstructure affecting mechanical properties and corrosion resistance of an al-9 wt% si alloy. *Materials and Manufacturing Processes*, **22**(3), 328–332 (doi: 10.1080/10426910701190345)

Park CL, Voorhees P and Thornton K (2015) Evolution of interfacial curvatures of a bicontinuous structure generated via nonconserved dynamics. *Acta Materialia*, **90**, 182–193 (doi: 10.1016/j.actamat.2022.117964)

Pinzer B, Schneebeli M and Kaempfer T (2012) Vapor flux and recrystallization during dry snow metamorphism under a steady temperature gradient as observed by time-lapse micro-tomography. *The Cryosphere*, **6**(5), 1141 (doi: 10.5194/tc-6-1141-2012)

Roberts AP and Garboczi EJ (2002) Computation of the linear elastic properties of random porous materials with a wide variety of microstructure. *Proceedings of the Royal Society of London. Series A: Mathematical, Physical and Engineering Sciences*, **458**(2021), 1033–1054 (doi: 10.1098/rspa.2001.0900)

Roberts AP and Knackstedt MA (1996) Structure-property correlations in model composite materials. *Phys. Rev. E*, **54**, 2313–2328 (doi: 10.1103/PhysRevE.54.2313)

Roberts AP and Teubner M (1995) Transport properties of heterogeneous materials derived from gaussian random fields: Bounds and simulation. *Phys. Rev. E*, **51**, 4141–4154 (doi: 10.1103/PhysRevE.51.4141)

Saito Y (1996) *Statistical physics of crystal growth*. World Scientific (doi: 10.1142/3261)

Schleef S and Loewe H (2013) X-ray microtomography analysis of isothermal densification of new snow under external mechanical stress. *Journal of Glaciology*, **59**(214), 233–243 (doi: 10.3189/2013JoG12J076)

Schroeder W, Martin K and Lorensen B (2006) *The visualization toolkit*. Kitware, 4 edition, ISBN 193093419X

Snyder V, Alkemper J, Voorhees P and Akaiwa N (1999) The influence of temperature gradients on ostwald ripening. *Metallurgical and Materials Transactions A*, **30**, 2341–2348 (doi: 10.1007/s11661-999-0243-1)

Soyarslan C, Bargmann S, Pradas M and Weissmüller J (2018) 3d stochastic bicontinuous microstructures: Generation, topology and elasticity. *Acta Materialia*, **149**, 326–340, ISSN 1359-6454 (doi: 10.1016/j.actamat.2018.01.005)

Taillandier AS, Domine F, Simpson WR, Sturm M and Douglas TA (2007) Rate of decrease of the specific surface area of dry snow: Isothermal and temperature gradient conditions. *Journal of Geophysical Research: Earth Surface*, **112**(F3) (doi: 10.1029/2006JF000514)

Tan S, Xiong C, Xu X and Tsang L (2016) Uniaxial effective permittivity of anisotropic bicontinuous random media using nmm3d. *IEEE Geoscience and Remote Sensing Letters*, **13**(8), 1168–1172 (doi: 10.1109/LGRS.2016.2574759)

Tuzet F, Dumont M, Lafaysse M, Picard G, Arnaud L, Voisin D, Lejeune Y, Charrois L, Nabat P and Morin S (2017) A multilayer physically based snowpack model simulating direct and indirect radiative impacts of light-absorbing impurities in snow. *The Cryosphere*, **11**(6), 2633–2653 (doi: 10.5194/tc-11-2633-2017)

Vionnet V, Brun E, Morin S, Boone A, Faroux S, Moigne P, Martin E and Willemet J (2011) The detailed snowpack scheme crocus and its implementation in surfex v7. *Geoscientific Model Development (submitted). submitted* (doi: 10.5194/gmd-5-773-2012)

Wagner C (1961) Theorie der Alterung von Niederschlägen durch Umlösen (Ostwald-Reifung). *Zeitschrift für Elektrochemie, Berichte der Bunsengesellschaft für physikalische Chemie*, **65**(7-8), 581–591 (doi: 10.1524/zpch.1963.36.5_6.292)

Wang X and Baker I (2014) Evolution of the specific surface area of snow during high-temperature gradient metamorphism. *Journal of Geophysical Research: Atmospheres*, **119**(24), 13–690 (doi: 10.1002/2014JD022131)

Wiese M and Schneebeli M (2017) Snowbreeder 5: a micro-ct device for measuring the snow-microstructure evolution under the simultaneous influence of a temperature gradient and compaction. *Journal of Glaciology*, **63**(238), 355–360 (doi: 10.1017/jog.2016.143)

Yan H, Wang K and Glicksman M (2022) Microstructural coarsening in dense binary systems. *Acta Materialia*, **233**, 117964 (doi: 10.1016/j.actamat.2022.117964)

Zelinka MD and Hartmann DL (2012) Climate feedbacks and their implications for poleward energy flux changes in a warming climate. *Journal of Climate*, **25**(2), 608 – 624 (doi: 10.1175/JCLI-D-11-00096.1)